Journal of Constructional Steel Research 194 (2022) 107305

Contents lists available at ScienceDirect

Journal of Constructional Steel Research

journal homepage: www.elsevier.com/locate/jcsr

Assessment of deformation in bridge bearing areas using measurements and welding simulation

D. Kollár [a,*], B. Kövesdi [a], I. Völgyi [a], I. Biró [b]

[a] Budapest University of Technology and Economics, Faculty of Civil Engineering, Department of Structural Engineering, Műegyetem rkp. 3., 1111 Budapest, Hungary
[b] Budapest University of Technology and Economics, Faculty of Mechanical Engineering, Department of Manufacturing Science and Engineering, Műegyetem rkp. 3., 1111 Budapest, Hungary

ARTICLE INFO

Keywords:
Structural bearing
Bridge superstructure
Welding simulation
Out-of-flatness
Coordinate measuring machine
Bearing area

ABSTRACT

Deformations of bottom flanges in the vicinity of bridge bearings, i.e., in bearing areas, due to manufacturing and loading can result in serious problems in service life and damages in bridge superstructures and structural bearings coming from nonuniform stress distribution. The paper focuses on the out-of-flatness measurement of bearing areas using Coordinate Measuring Machine (CMM) in typical steel and composite bridges having box and open cross-sections. Advanced manufacturing simulations are also carried out in addition to site measurements to analyse imperfections due to welding during assembly and strengthening of a typical bridge superstructure. A qualitative comparison is made with measurement results showing that the magnitudes of simulated and measured distortions are in good agreement. Results are evaluated in accordance with the permitted total deformation limit in EN 1337–2 recommended for spherical structural bearings. The current study uses a novel approach in the field of bridge engineering; the analogy of Abbott-Firestone curve is applied for describing the deformed shape and evaluating the extent of defects in the contact area since the magnitude of out-of-flatness imperfection is not inevitably sufficient for classifying the surfaces. Based on the obtained results it is demonstrated that using additional transverse bearing stiffeners for strengthening the superstructure can result in large distortions. Even the magnitude of out-of-flatness due to welding of transverse bearing stiffeners can exceed the permitted limit resulting in nonuniform stress distribution in the sliding elements affecting wear resistance and service life of spherical structural bearings.

1. Introduction

Structural bearings are essential elements of the load bearing behaviour of bridges by transferring vertical and horizontal loads between superstructure and substructure. However, requirements of design standards regarding rotations, displacements and loads need to be fulfilled. Bridge construction technologies frequently demand the installation of structural bearings after the erection of the superstructure, while posterior placing of bearings is requisite as well in the case of bearing replacements. Manufacturing tolerances of bearings and general requirements in Europe are given in EN 1337-1 [1], while regulations regarding specific bearing types are introduced in subsequent parts of EN 1337 (EN 1337-3 – EN 1337-8). Spherical bearings, which are widely used in bridge engineering and are introduced in EN 1337-7 [2], consist of precision machined components with low surface roughness (e.g., backing plates with convex and concave spherical surfaces) allowing relative displacements and sliding elements made of special materials such as polytetrafluorethylene (PTFE), ultrahigh molecular weight polyethylene (UHMWPE) or composite materials ensuring low friction coefficients and minimizing the effect of wear. Ultrahigh molecular weight polyethylene is mainly used in novel structural bearings since it has significantly higher compressive strength resulting in smaller dimensions, high-performance and improved lifetime. Characteristics for the design and manufacture of sliding elements, with a maximum diameter of 1500 mm, are defined in EN 1337-2 [3], while this part refers to installation deviations as well. On the other hand, EN 1337-11 [4] partially focuses on specific installation instructions and installation tolerances of structural bearings. Specifications are relatively brief, and the interpretation is not trivial.

Generally, there are not any detailed installation manual widely available for structural bearings; therefore, instructions of the standards are authoritative in most of the cases. EN 1337-11 discusses the general

* Corresponding author.
E-mail address: kollar.denes@emk.bme.hu (D. Kollár).

https://doi.org/10.1016/j.jcsr.2022.107305
Received 8 February 2022; Received in revised form 20 April 2022; Accepted 28 April 2022
Available online 14 May 2022

principles of forming the contact surface between structural bearing and substructure. Bearings shall be supported on the entire contact surface irrespectively of the method used for installing mortar (cambered bed, pouring, grouting, etc.). Zones with variable rigidity subjected to compression shall be avoided underneath or on the structural bearings according to EN 1993-2 [5] A.5.7, while grouting or machined plates are recommended to use for levelling purposes. However, substantive directives are not introduced for installing tolerances in the standard. Maximum permitted deviations from theoretical plane or curved surfaces for backing plates and sliding surfaces shall not exceed 0.03% of the characteristic dimension of the component or 0.2 mm as given in EN 1337-2 [3].

Permitted total deformation limit ($\Delta w_1 + \Delta w_2$) of adjacent backing plates (Fig. 1) is given by EN 1337-2 in order to avoid higher wear of the contact surfaces which affects the long-term fitness of sliding elements; therefore, this condition is generally treated as serviceability limit state. The permitted deformation is defined as follows in Eq. 1:

$$\Delta w_1 + \Delta w_2 \leq h\left[0.45\text{–}2(h/D)^{0.5}\right] \tag{1}$$

where h is protrusion of the sliding element from the backing plate, while D is the diameter of the sliding element. In addition, stresses in the backing plates induced by the aforementioned deformation limit should not result in plastic deformations. Simplified formulae and general principles for common materials are also given in Annex C of the standard for calculating deformation component Δw_1. As a simplification, deformation component Δw_2 may be evaluated using the theory of elastic circular plates (i.e., sliding element) and pressure distributions (constant or parabolic) given in the standard. However, numerous assumptions, such as central load or linear elastic material model for the sliding element, are made which limits the applicability of the method. It is also recommended in the standard to reduce the elastic modulus of concrete or mortar linearly from the edge of the backing plate to the centre from 100% to 80%, due to nonuniform grout consistency and stiffness, resulting in an unfavourable imperfection of the contact surface. Numerical methods, e.g., finite element method, provide cutting-edge technologies in order to overcome the limitations of simplified approaches and perform detailed analysis of the interaction of superstructure or substructure and structural bearing [6–8]. Out-of-flatness tolerance for the contact surfaces of structural bearings and superstructure is not given in EN 1337. On the other hand, additional specifications are defined for the geometrical imperfections of the superstructure in the vicinity of supports. Manufacturing and erection tolerances are given in Annex B in EN 1090–2 [9] permitting relatively large imperfections in the contact area of the structural bearing. Manufacturing tolerances for stiffened plates are defined in Table B.7. Essential imperfections and the corresponding manufacturing tolerances of transversely stiffened plates, such as the bottom flange of a box girder with a diaphragm, affecting the interaction of the structural bearing and the superstructure are summarized in Table 1. The permitted deviation of straightness perpendicular to the bottom flange, projected to the contact area, is typically 0÷3 mm for class 2 (execution classes 3 and 4) with increased requirement strictness assuming sliding elements with a maximum diameter of 1500 mm. Permitted vertical deviation relative to adjacent transverse stiffeners and diaphragms is typically $\pm L/400$ or $\pm L/500$ which yields imperfections with a magnitude of 0÷2 mm in the contact area of common spherical bearings.

Bending stiffness of the superstructure is larger than the stiffness of structural bearings by orders of magnitude; thus, imperfections of the bottom flange will constrain the structural bearing and result in additional deformation. Supplementary rules are given in EN 1993–2 [5] A.5.1 for sliding elements introducing that deformation components in *Eq. 1* include the effect of imperfections and elastic deformation as well. Tolerances described above clearly show that imperfections of connecting structures may significantly exceed permitted total deformations and affect the structural behaviour of bearings.

Nevertheless, some additional instructions can be found in the literature. An installation guide of VHFL (Vereinigung der Hersteller von Fahrbahnübergängen und Lagern für Bauwerke) [10] is available in Germany, which also recommends out-of-flatness tolerance for the adjacent superstructure surface with a maximum of 0.03% of the connected bearing plate diameter for sliding bearings. Additionally, polymer-bound metal (e.g., DIAMANT MM1018 or equivalent) is specified for the compensation of inaccuracies and imperfections of contact surfaces. Some structural bearing manufacturers (e.g., Mageba) recommend additional tolerances for the out-of-flatness of the lower surface of the superstructure. The specified tolerance is quasi-equivalent with the VHFL guideline. However, the scope of these guidelines and instructions is not general; furthermore, these instructions are not obligatory for construction companies.

Coordinate measurement methods can be useful to determine the scale and type of geometrical imperfections and deformations. Coordinate measurement applications can be classified according to the principle of measurement:

a) Contact dimensional inspection (tactile): the tester is in direct physical contact with the measured surface. The acquisition of position data by a tactile tester is triggered by the contact force (detected by piezoelectric sensors or strain gauges), or by optical (fiber-probe) and electric-mechanical (coupler) means [11].
b) Non-contact dimensional inspection: there is no physical contact between the detected surface and the tester. Data capture can be based on optical (i.e. reflection during measurement by laser-scanners) and tomographic (i.e., emission during computed tomographic measurements) principles [11–13].

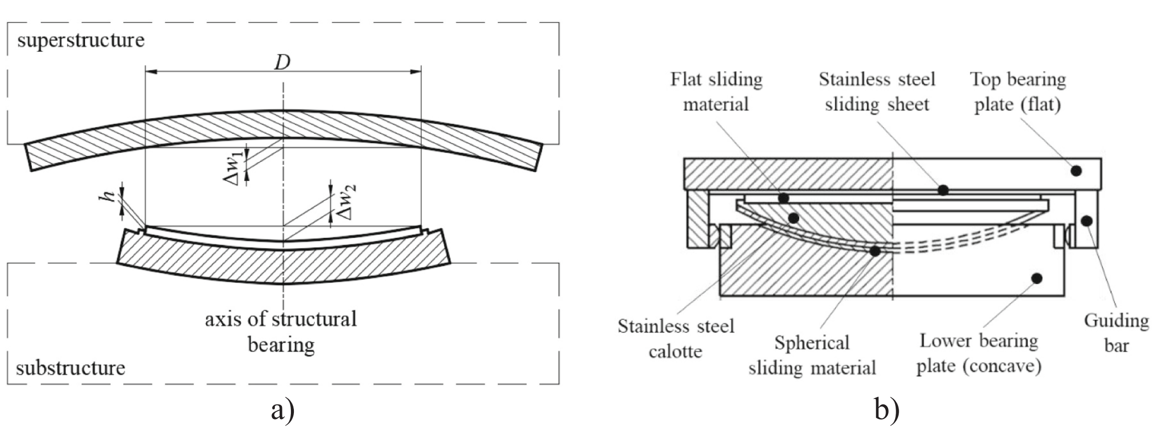

Fig. 1. a) Deformation components of backing plates according to EN 1337-2 [3] and b) a guided spherical bearing based on EN 1337-7 [2].

Table 1
Manufacturing tolerances of transverse stiffeners in transversely stiffened plates according to EN 1090–2 [9].

Criterion	Parameter	Permitted deviation Δ		
		Essential tolerances	Functional tolerances	
		Class 1 and 2	Class 1	Class 2
Straightness of stiffeners	Out-of-plane deviation Δ 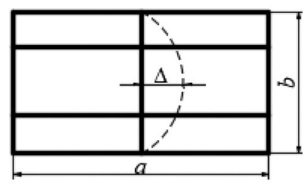 Deviation Δ perpendicular to the plate 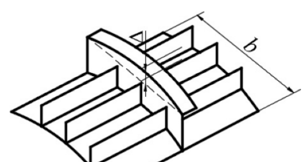	± min(a, b)/400	± min(a, b)/400	± min(a/500, b/750), but $\|\Delta\| \geq 2$ mm
Levels of cross members in stiffened plates	Level relative to the adjacent cross frames 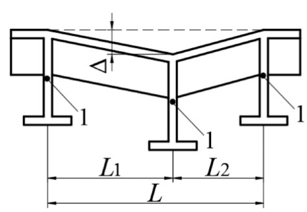 1 - cross member	± L/400	± L/400	± L/500, but $\|\Delta\| \geq 3$ mm

In the case of tactile measurements, the calibration of the tester's position within the standard coordinate system of the measuring machine is essential, including the determination of the correction parameters related to the tester's width and length. Due to the simplistic measuring method, coordinate measurement is a well-applied asset of quality control in general part manufacturing and assembly operations on the industrial level as well, directly mentioning precision part manufacturing [14,15], and the automotive [16] and medical industries [11,17]. Standard Coordinate Measuring Machines (CMMs) are massive stand-alone structures suitable for performing high-volume and automated precision measurements in industrial and laboratory circumstances, as demonstrated by the authors [18]. A similar application in 2019 has successfully realised the determination of welding-induced distortions of small-scale T-joints of stator segments. A generally applied version of CMMs is the bridge-type machine, which can move the tactile tester along with the directions of three-dimensional space of Euclidean geometry [19] (including movements generated by linear orthogonal transformation [12], if the tester can be rotated). Thus, the measurement has a rectangular range, while the part is placed on a solid table. Weight and size of parts fundamentally limit the application of CMMs, as they must be under the maximum allowed rate. The Articulated Arm Coordinate Measuring Machines (AACMMs) are the portable versions of CMMs. Although they are less robust and typically have a more limited range of measurement due to their construction, they can be effectively applied for on-field measurements. They do not require any part-holding table; thus, the part's weight and size does not limit the operation. Furthermore, AACMMs can be transported to the location of the measurement, making the testing of built-in components realisable. AACMMs are articulated by rotating joints, which usually provide a spherical range of measurement. Due to its construction, measurements by AACMM are fundamentally based on linear orthogonal transformation (most notably on rotation [18,19]). Non-contact dimensional inspections also have a significant role in coordinate measurement applications. Tomographic measurements are suitable for detecting undercut (or hidden) surfaces, though they require a specialised and shielded inspection area due to the dangers of the applied X-rays [20]. Optical scanning proves to be less circumstantial from the point of deployability. However, the surface quality (most notably the optical properties) affects the effectiveness and accuracy of the data capture by an optical, and the relatively high volume of data requires significantly more computational resources as compared to contact dimensional measurements. Generally speaking, non-contact measurement methods can be effectively deployed to capture large-scale objects such as civil engineering structures (e.g., bridges [21] and street sections [22]), and smaller sub-structures. A direct example for on-location 3D scanning has been demonstrated by Piculin and Može [23] in 2020, who measured the out-of-flatness initial imperfections of test specimens, stiffened curved plates as bottom flanges of steel bridges, in laboratory by structured light portable 3D scanner.

The paper is also focusing on the modelling aspects of manufacturing simulations regarding large-scale structures and especially bridge engineering examples. Pasternak et al. [24] proposed a combined analytical-numerical hybrid shrinkage model in 2017 for simplified welding simulations of large components using inherent strain due to welding. The proposed approach takes both welding-induced deformations and residual stresses into account. The method is presented on an I-girder; however, it can be extended for different structural applications. Krausche et al. [25] used the macro bead deposit method (or lump-pass analysis) in 2017, in order to reduce computation time and determine the effect of different welding sequences in the case of a box section with a unique shape and stiffeners. Residual stresses were comparable; however, distortions were qualitatively different for variant welding sequences. Van Puymbroek et al. [26] also dealt with the welding simulation of a stiffener-to-deck plate detail of an orthotropic steel deck in 2019. Residual stress results were validated by experimental measurements by using the so-called incremental hole-drilling method. Zhang et al. [27] performed experimental investigation and numerical simulation on welding-induced residual stresses of innovative double-side welded rib-to-deck joints of orthotropic steel decks in 2021 using local models, while the influence of geometrical parameters and welding variables on residual stresses were numerically studied. A local model was applied as well by Wu et al. [28] in 2022 for the numerical simulation of welding-induced residual stresses in orthotropic steel decks with diaphragm considering solid-state phase transformation, while hole-drilling method was used for residual stress measurements. Hashemzadeh, Garbatov and Guedes Soares [29] was dealing with the thermo-mechanical modelling of hybrid-laser welding-induced distortions and residual stresses of a large-scale ship deck panel in 2022 by implementing a simplified heat source model. The analysed stiffened panel, with HP80 × 5 stiffeners, had a length of 3360 mm and a width of 540 mm representing a typical thin deck structure of a cruise ship.

A comprehensive literature review is carried out focusing on the directives of design and layout of contact surfaces, imperfection measurements and manufacturing simulations regarding large-scale structures and bridge engineering examples. However, it can be concluded that, according to the authors' knowledge, the international literature is barely dealing with the topic of out-of-flatness of bottom flanges in bridge superstructures in the vicinity of structural bearings. Nevertheless, it is one of the possible causes of damages and failure of structural bearings. The novelty and relevance of the current research can be summarized as follows:

- magnitudes and characteristics of typical imperfections of contact surfaces, affecting behaviour of structural bearings, are measured using CMM which has not been published yet in the international literature,
- analogy of Abbott-Firestone curve is applied to describe the deformed shape of the contact area which is a novel application of an established approach in the field of bridge engineering for evaluating such a problem,
- a comprehensive nonlinear three-dimensional finite element model is developed for manufacturing simulations to analyse the influence of welding on distortions in the vicinity of structural bearings during the assembly and strengthening due to retrofitting of a typical superstructure,
- influence of superstructure stiffness on contact surface imperfection is evaluated, using both measurements and simulations, which has a fundamental effect on the behaviour and damages of spherical bearings,
- effects of manufacturing technology, cross-section type and erection period are clarified.

2. CMM measurements

2.1. Measurement strategy

Road and railway bridges involved in the research are chosen to represent typical steel and composite bridges manufactured in Central Europe. Box section and open section bridges, erected in the last decades of the 20th century and in the 21st century including recent years, are analysed. The welded joint and the thickness of bottom flange and diaphragm near the contact surface of structural bearings depend significantly on the cross-section type. The influence of plate thickness, i.e., cross-section type, on welding-induced distortions is analysed, while the relation between measured imperfections and development of welding technology in the last decades is also assessed. Typical bridges with open and box sections are investigated (Fig. 2) having different structural layout in the vicinity of supports. Differences in the structural layout have significant impact on deformations and out-of-flatness of the bottom flange. In the case of open section bridges, a relatively thick bottom flange with higher stiffness is used, while web plates, diaphragms and bearing stiffeners of cross-girders and main girder are much thinner in general, which require lower heat input during welding than in most of the bridges with box sections where the diaphragm has larger thickness, and a relatively thin longitudinally stiffened plate is used as bottom flange. Thickness of relevant plates (diaphragm, bearing stiffeners, web and bottom flange) and the weld type between these plates have the most important effect on the analysed out-of-flatness distortions. Approximate characteristic data and additional information of bridges involved in the research are summarized in Table 2. End supports and mid supports are also analysed in the research program. Bridges are sorted in two subgroups of superstructures with box sections (Bridges #1–5) and with open cross-sections (Bridges #6 and #7).

2.2. Measurement system and postprocessing

Deformations of structural bearing backing plates have been determined by point clouds acquired by a FARO Gage Plus (type F04) AACMM (Fig. 3a). According to EN ISO 10360-2 [30] the accuracy of the measurement can be described by two parameters, which have been calibrated by the manufacturer. Length measurement error E_L is the expected length deviance of the absolute distance L of the captured point from the active reference (i.e., local coordinate system) determined by the captured X, Y and Z coordinates (Fig. 5a). The measurement range is $L_{max} = 1200$ mm (Fig. 3b), while the maximum permissible error of length measurement of the gage is $E_{L,MPE} = \pm 15$ μm. Repeatability range of the length measurement error R_0 is the expected form deviance of a best-fitted surface on a captured point cloud. It means that the form tolerance of the measured surface should be greater than R_0 in order to regard the evaluated form error relevant, i.e., the tolerance of form must be greater than the uncertainty of the measurement (Fig. 5b). The volumetric probing uncertainty of the applied AACMM is $R_0 = 6$ μm. Data of the captured point clouds are registered and preliminarily evaluated by FARO CAM2 SmartInspect software. The aim of the measurements is to determine the out-of-flatness surface profile of bottom flanges. The process of data capturing comprises the following steps:

1. *Determination of the local coordinate system.* Fig. 3b represents the standard measurement setup. Due to sections of the blacking plates being out of the AACMM's measurement range and the limited space to fix and operate the gage, each backing plate has to be measured in multiple positions; thus, repositioning of the AACMM is unavoidable. Local coordinate systems are identified for each individual position, and they are aligned to local structural elements (e.g., diaphragm) in order to represent the orientation of the plate (Fig. 4). Thereby, a common reference for the point clouds can be provided
2. *Acquiring a point cloud.* Points are acquired by an offset of $\Delta X = \Delta Y =$ 30…50 mm along a laced path (Fig. 4). Positioning of the probe and data capture are realised manually. Position measurement of a point has two types of uncertainty. Expected errors are the calibrated uncertainties of the gage, namely the length measurement error (E_L on Fig. 5a). Unexpected (or coincidence) error exists due to the quality of measured surfaces and manual positioning. The surface can have relevant inhomogeneity because of the worn state of the surface layer, corrosion, paint sagging (causing uneven cover layer on the plates), and the presence of welding spatter. The relative effect of unexpected errors can be reduced by acquiring more points in the critical areas
3. *Preliminary on-the-spot evaluation of data.* The FARO CAM2 SmartInspect software is suitable for performing real-time evaluation and visualization of the currently captured data. In the case of storing at least three measured points, the automated plane fitting is an

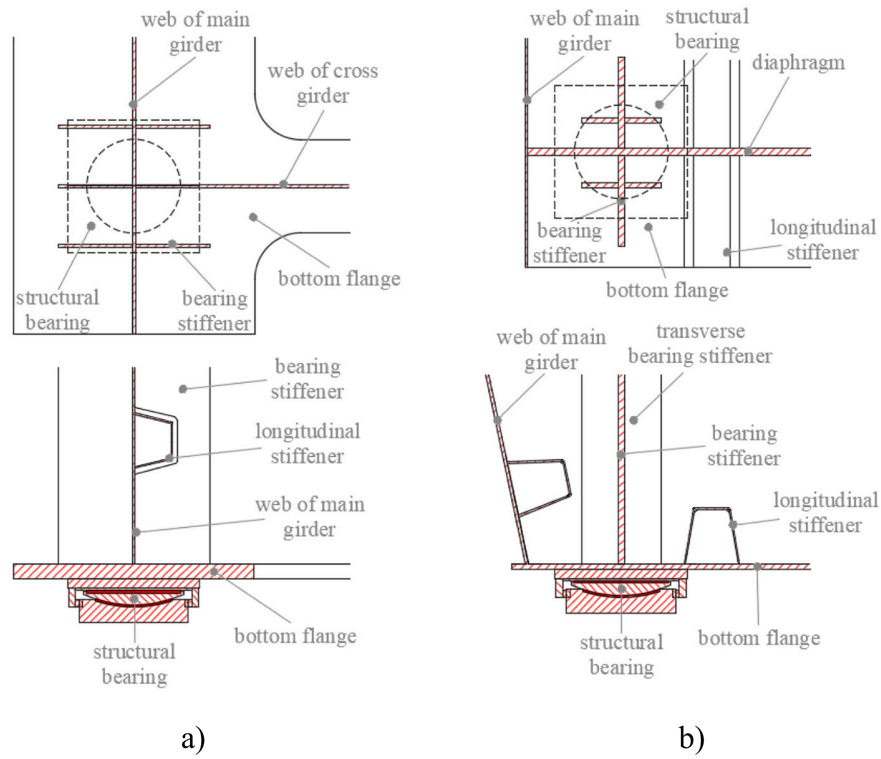

Fig. 2. Layout of a) open and b) box sections near structural bearings.

Table 2
Characteristic data of analysed bridges (*approximate value).

	Subgroup #1: Box section					Subgroup #2: Open section	
Data	Bridge #1	Bridge #2	Bridge #3	Bridge #4	Bridge #5	Bridge #6	Bridge #7
Bridge type	Continuous girder	Continuous girder	Continuous girder	Continuous girder	Continuous girder	Cable-stayed	Continuous girder
Traffic	Road	Road	Road	Road	Road	Road	Railway
Material	Composite	Composite	Composite	Steel	Steel	Steel	Steel
Cross-section	Single-cell box girder	Single-cell box girder	Single-cell box girder	Single-cell box girder	Double-cell box girder	Orthotropic deck, two main beams	Truss girder
Span* [m]	3 × 110	3 × 75	3 × 75	95 + 145 + 95	50 + 4 × 100 + 50	65 + 250 + 120 + 95 + 65	50 + 4 × 100 + 50
Width* [m]	22	22	22	34	31	20	8
Location of measurements	Internal support	Internal support	Internal support	Internal support	End support	End support	End support
Structural bearing distance* [m]	8.0	8.0	8.0	5.5	12.5	15.3	5.2
Thickness of bottom flange [mm]	30	16	16	45	12	40	40
Thickness of web [mm]	30	16	16	20	12	16	30
Thickness of diaphragm [mm]	30	30	40	40	20	20	20
Maximum thickness of stiffeners [mm]	40	30	30	30	20	16	20
Weld type between bottom flange and web	Double-sided fillet weld	Double-sided fillet weld	Double-sided fillet weld	Double-sided fillet weld	Double-sided fillet weld	Double-sided fillet weld	Double-sided fillet weld
Weld type between bottom flange and plates (excl. web)	Double-bevel groove weld	Double-bevel groove weld	Double-bevel groove weld	Double-bevel groove weld	Double-bevel groove weld	Double-bevel groove weld	Double-bevel groove weld
Erection technology	Temporary supports, concrete casting at side spans, lowering supports		Temporary supports, concrete casting at side spans	Lifting entire span	Lifting entire span	Temporary supports	Temporary supports
Erection period*	1990	1990	2010	2010	1990	2020	2020
Manufacturing site	Hungary	Hungary	Hungary	Hungary	Hungary	Poland	Poland / Slovakia

available function. Based on the least-squares method, the best fitting plane can be determined (Fig. 5a). Out-of-flatness F of the measured surface is represented by the extend of points parallel to the $\underline{n}$ normal vector of the best-fitted plane (Fig. 5b). The following issues are checked during the real-time evaluation: (i) out-of-flatness F can be regarded relevant if it exceeds the volumetric probing

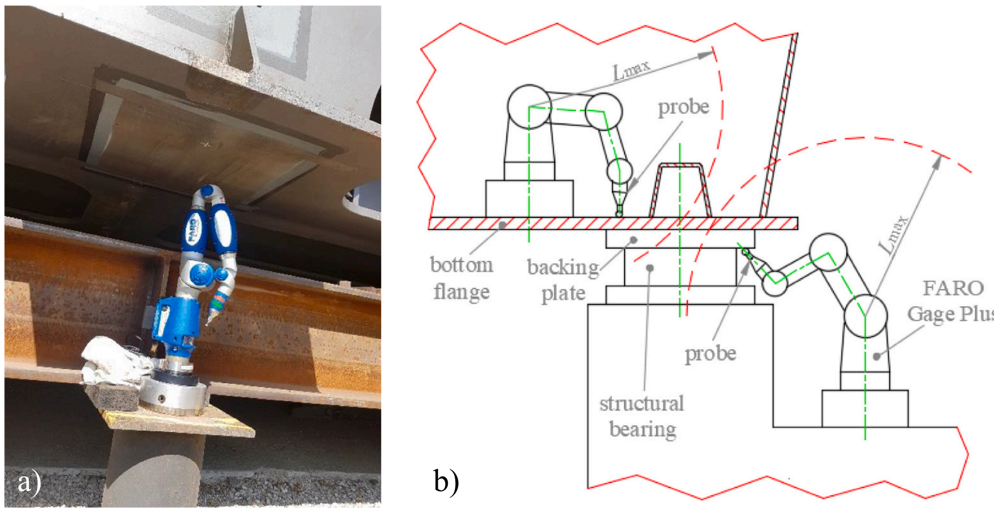

Fig. 3. a) Measurement setup on site and b) measurement of a backing plate (from beneath) and bottom flange (from above).

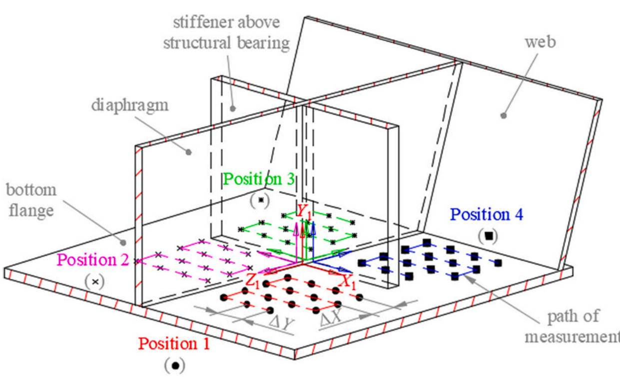

Fig. 4. Local coordinate systems and data capture strategy of a bottom flange.

uncertainty ($F >> R_0$), and (ii) if a jump in the value of F is observed, a false measurement may have been carried out due to an unexpected error. In such a case, false data are deleted, and the measurement can be continued by adding new points to the cloud.

4. *Addition of more points (if required)*. Based on the observation and conclusion made according to the preliminary evaluation, the already registered point cloud can be extended by adding new measurements. However, this is only realisable until the AACMM remains in the same position as during the original measuring session; otherwise, the common reference of the original point cloud and the additional points is lost.
5. *Posterior evaluation of data*. Due to multiple positions, posterior evaluation of data is necessary, which is carried out in MATLAB in order to transform data points in various local coordinate systems into a common local coordinate system. For instance, data capturing is carried out on both sides of a diaphragm resulting in a required transformation of point clouds. Therefore, reference points and planes are defined during data capturing, making it possible to determine out-of-flatness imperfections for the entire data cloud. Thin-plate smoothing spline, a special case of a polyharmonic spline, is used in the software to interpolate surfaces over scattered data and smoothing. The name of the spline-based algorithm refers to the physical analogy of bending energy of a thin sheet on point constraints. According to Bookstein [31], the bending energy for interpolation of a surface over a fixed set of nodes in the plane is a quadratic form in the heights assigned to the surface, while the spline function is the superposition of eigenvectors of the bending energy matrix. A smoothing parameter p varies from 0 to 1 and can be adjusted in order to set the level of smoothing. Thus, the smoothing spline varies from the least-squares approximation by a linear polynomial when $p = 0$ to the thin-plate spline interpolant when $p = 1$. Thin-plate smoothing is performed by solving a linear system resulting in a closed-form solution. The smoothing parameter p provided by the software is used in the analysed cases in such a way that the thin-plate smoothing spline f is the unique minimizer of the weighted sum $\xi pE(f) + (1 - p)R(f)$ where $E(f)$ is the error measure, R

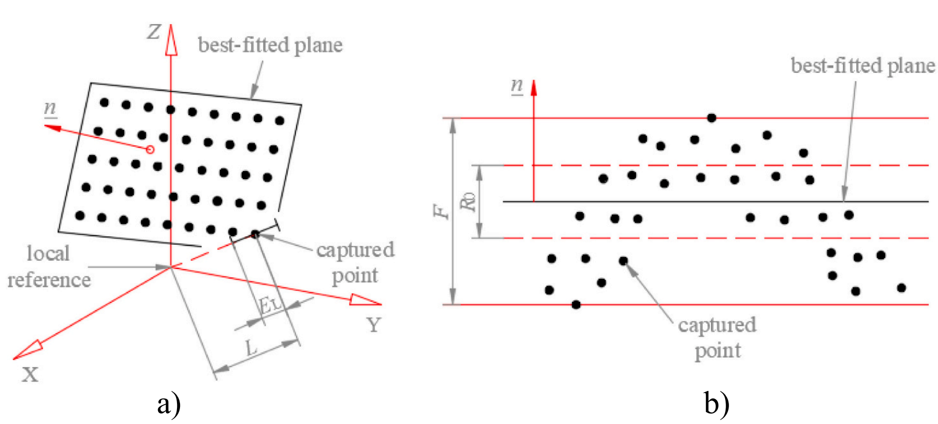

Fig. 5. Flatness probing by AACMM: a) point cloud and best-fitted plane and b) parameters of expected uncertainty and out-of-flatness.

(f) is the roughness measure in the evaluation. Regression plane is determined afterwards using least-squares approximation.

Data evaluation is performed assuming contact surfaces with different diameters ($D = 200$ mm, 300 mm, 400 mm, and 500 mm); thus, measurement results can be compared for various bridge structures. Corresponding permitted total deformation limits are 0.53 mm, 0.61 mm, 0.66 mm, and 0.70 mm, respectively with protrusion size $h = 1.75$ mm + $D/1200$, but not less than 2.2 mm according to the recommendations of EN 1337–2. In addition, out-of-flatness measurement results are normalized in order to make a reasonable comparison for the different structural configurations. It is to be highlighted in some cases it is not feasible to perform measurements for the entire surface due to structural restrictions such as not sufficient measurement space because of longitudinal stiffeners, etc. After thin-plate smoothing, translational and rotational transformation of the fitted data set is carried out in order to find the three interfacing points representing each contact surface and determine characteristic parameters such as maximum out-of-flatness. In addition, the analogy of Abbott-Firestone curves [32] is used describing and evaluating the surface texture as well for each scenario. From a mathematical point of view, Abbott-Firestone curve (*Fig. 6*) is the cumulative distribution function of the surface profile (i.e., out-of-flatness in the current paper). However, it is generally used as bearing area curves in roughness measurements and the curve denotes specific surface roughness parameters such as core roughness depth, reduced peak height and valley depth, material ratios, etc. In the current paper, areal material ratio (bearing area) $S_{mr}(c)$ at a specified out-of-flatness c (Fig. 6) is used according to ISO 25178-2, where c denotes the permitted total deformation limit $\Delta w_1 + \Delta w_2$ for each measured case. In addition, minimum secant slope $\tan(\alpha)$ is also determined using two points separated by 40% on the horizontal axis and shifted along the curve in order to evaluate the minimum slope according to the standard.

2.3. Measurement results

Measured and analysed out-of-flatness results, for the entire measured surfaces, are plotted for both subgroups of bridges with box (Fig. 2a) and open (Fig. 2b) cross-section. Out-of-flatness profiles are also evaluated at several specific longitudinal and transverse sections (denoted with continuous black lines with a scale of 25) to visualize typical distortions due to manufacturing and loading. In addition, bearing stiffeners and the diaphragm are also shown with light patched polygons to introduce the layout of the superstructure in the vicinity of the structural bearing. Positive (reddish colours) and negative values (bluish colours) in the figures, representing measured out-of-flatness results, indicate convex and concave imperfection shapes from the top. Measurement results for box sections are shown in Fig. 7. Similar distorted shapes, with two or three dimples in the quadrants defined by the diaphragm and the bearing stiffeners, are measured for Bridges #1–3 where bottom flange thickness varies between 16 mm and 30 mm, while maximum out-of-flatness is 4.4 mm, 5.2 mm (and 4.8 mm), and 3.4 mm,

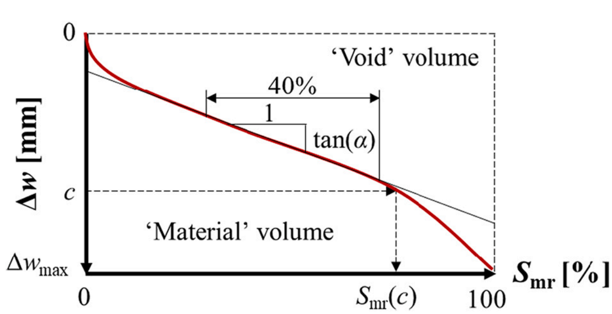

Fig. 6. A typical Abbott-Firestone curve, with bearing area S_{mr}(c) and minimum secant slope tan(α), transformed for out-of-flatness (Δw) measurements.

respectively. It is noted that surface profiles of two internal supports are plotted for Bridge #2. Erection period was between 1990 and 2010; however, solely a slight decrease in imperfections can be measured which does not seem to be an unequivocal correlation with the development of manufacturing and welding technology. Bridge #4, erected around 2010, has a bottom flange with a relatively large plate thickness of 45 mm in point of bridges with box sections resulting in smaller imperfections; namely maximum out-of-flatness is 2.6 mm, while only one relevant dimple is measured in one of the quadrants. Bridge #5 was erected around 1990 and the corresponding flange thickness is 12 mm; however, only one major dimple is measured with a maximum out-of-flatness of 2.4 mm in the centre denoted by the intersection of diaphragm and bearing stiffeners above the support. Fairly small bearing stiffeners, with cross-section of 240 × 20, are welded to the diaphragm and bottom flange which explains smaller welding-induced imperfections due to lower total heat transmitted into the structure compared to Bridges #1–3, where bearing stiffeners with cross-section of 500 × 30 are used. All the plotted measurements in the figure correspond to internal supports, except Bridge #5, where the vicinity of an end support is shown.

Bridges with open sections are introduced in Fig. 8. Near the end support, the surface profile regarding the bottom flange of Bridge #6, road bridge erected in 2020, shows an uncharacteristic shape with a maximum out-of-flatness of 2.6 mm. The measured surface has a width of 1200 mm and a length of 1400 mm, while a dimple with a magnitude of 1.2 mm is observed near the centre. An internal and an end support of Bridge #7 is measured; maximum out-of-flatness of 0.9 mm is evaluated near the centre for both surfaces with only one specific dimple. Bottom flange thickness is 40 mm for both bridges. Furthermore, it must be highlighted that Bridge #7 is measured during the assembly; therefore, elastic deformation due to reaction forces is not included in this case. Measurement data are summarized in Table 3 including maximum out-of-flatness (Δw_{max}), number of measured dimples (n_{dimple}), thickness of bottom flange (t_f), and maximum out-of-flatness-to-flange thickness ratio ($\Delta w_{max}/t_f$). The table clearly shows that flange thickness has an important effect on distortions and the relative magnitude of distortions is much smaller for bridges with open sections. Bridge #4 is an exception in the case of bridges with box sections; however, thickness of bottom flange is significantly larger than any other in this subgroup.

Normalized out-of-flatness (Δw_{norm}) measurement results are introduced for evaluation diameters $D = 200$ mm, 300 mm, 400 mm, and 500 mm to analyse and compare the distinct bridge structures in detail. Permitted total deformation limits are applied as denominator for normalization, while magnitudes are $\Delta w_1 + \Delta w_2 = 0.53$ mm, 0.61 mm, 0.66 mm and 0.70 mm, respectively. Examples for typical superstructures with box and open cross-sections are shown in Fig. 9 for $D = 400$ mm. Coincident surface profiles are shown for the circular contact surfaces as for the global behaviour; three dimples are evolving in the quadrants for the box section bridge with thin flange plate and longitudinal stiffeners, while only one characteristic dimple is measured in this region for a bridge with open section. Normalized out-of-flatness is plotted; therefore, zones with a magnitude above 1.00 represent that the bearing area may not ensure a suitable contact between the superstructure and structural bearing without using any levelling approach (e.g., mortar, machined plate, etc.) since the permitted total deformation limit is exceeded. Isolines representing 1.00 (thus, $\Delta w_1 + \Delta w_2$) are plotted with continuous black lines as well to denote regions not fulfilling the recommendations of EN 1337–2. It is pointed out that in the presented cases the bridge with box section has extremely large normalized out-of-flatness, namely more than 5, while it is around 1.5 for the open section. Normalized out-of-flatness results are summarized in Table 4 for each bridge. Maximum normalized out-of-flatness ($\Delta w_{norm,max}$) results (plotted in Fig. 10 as well), bearing areas (S_{mr}) evaluated at the permitted total deformation limit ($\Delta w_1 + \Delta w_2$), and minimum secant slopes ($\tan(\alpha)$) are tabulated. A total of thirty-six normalized Abbott-Firestone curves, which is used for determining the

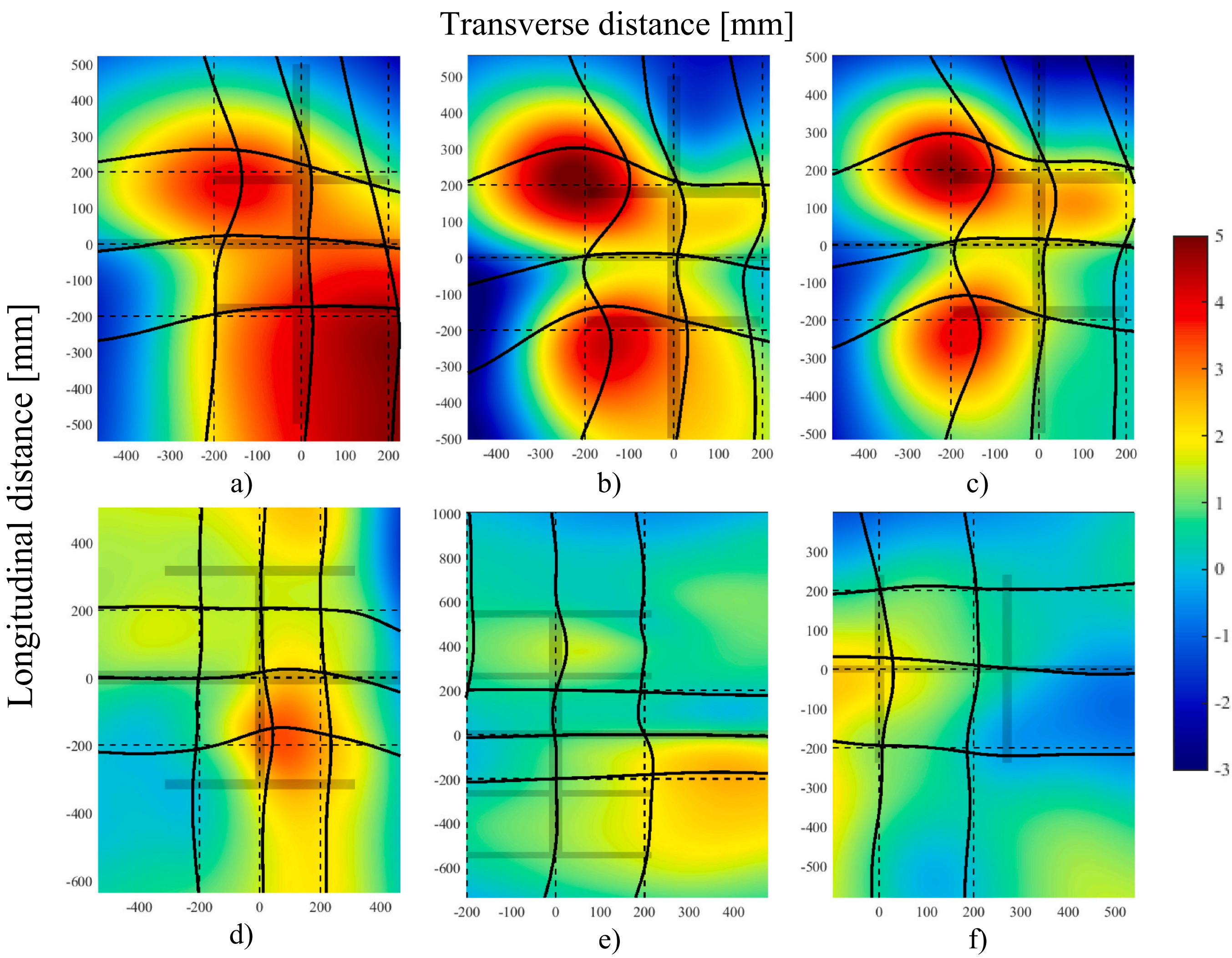

Fig. 7. Measured out-of-flatness [mm] results for bridges with box section: a) Bridge #1, b-c) Bridge #2, d) Bridge #3, e) Bridge #4 and f) Bridge 5.

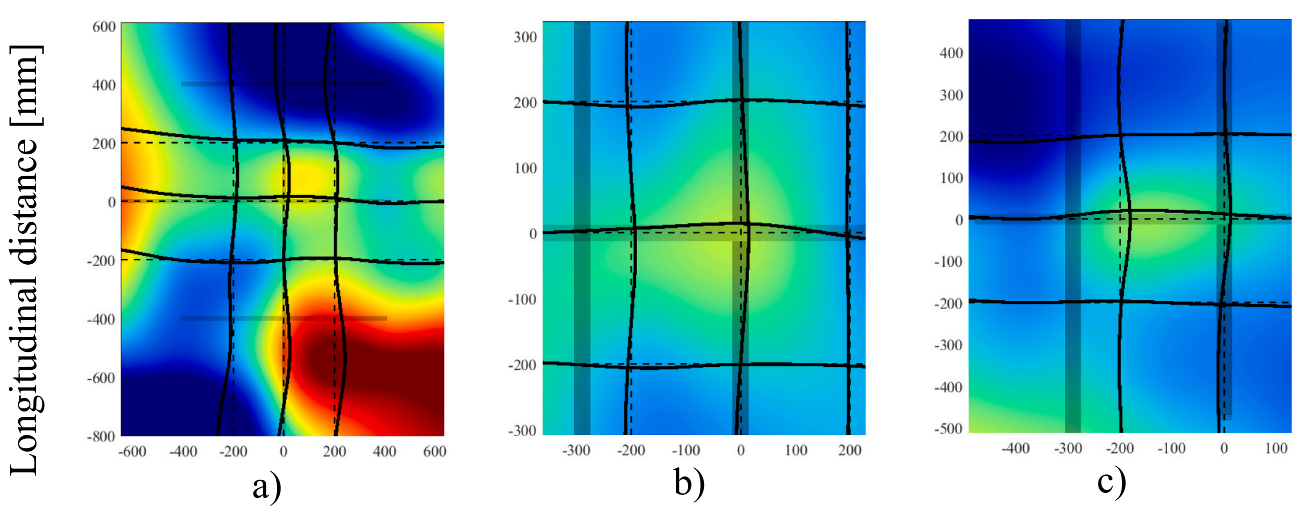

Fig. 8. Measured out-of-flatness [mm] results for bridges with open section: a) Bridge #6 (internal support) and b-c) Bridge #7 (internal and end support).

specific S_{mr} and $\tan(\alpha)$ values and reveal the differences between surface profiles, are shown in Figs. 11 and 12 for the seven analysed bridges (two internal supports for Bridge #2 and internal and end supports for Bridge #7) and four diameters. It can be demonstrated and clarified based on Abbott-Firestone curve shapes and normalized out-of-flatness magnitudes that bridges with box sections and open sections have fairly different out-of-flatness surface profiles. Generally, S-shape curves define the surface profiles for box sections, which is typical for Gaussian

Table 3
Measured out-of-flatness data of analysed bridges.

Data	Subgroup #1: Box section						Subgroup #2: Open section		
	Bridge #1	Bridge #2		Bridge #3	Bridge #4	Bridge #5	Bridge #6	Bridge #7	
		Internal	Internal					Internal	End
Δw_{max} [mm]	4.4	5.2	4.8	3.4	2.6	2.4	2.6	0.9	0.9
n_{dimple} [−]	2	3	3	1	1	1	–	1	1
t_f [mm]	30	16	16	16	45	12	40	40	40
$\Delta w_{max}/t_f$ [−]	0.147	0.325	0.300	0.213	0.058	0.200	0.065	0.023	0.023

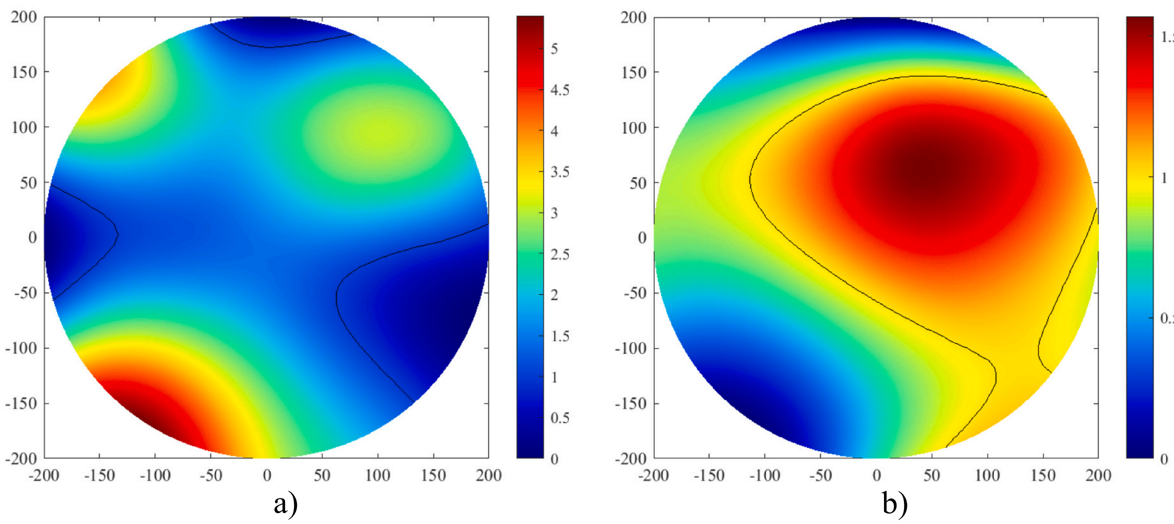

Fig. 9. Typical normalized out-of-flatness [−] results for bridges with a) box (Bridge #2) and b) open section (Bridge #6), D = 400 mm, and $\Delta w_1 + \Delta w_2 = 0.66$ mm.

Table 4
Normalized out-of-flatness results of contact surfaces for analysed bridges.

Data	D [mm]	Subgroup #1: Box section						Subgroup #2: Open section		
		Bridge #1	Bridge #2		Bridge #3	Bridge #4	Bridge #5	Bridge #6	Bridge #7	
			Internal	Internal					Internal	End
$\Delta w_{norm,max}$ [−]	200	1.18	2.05	1.92	1.11	0.70	0.96	0.31	0.44	0.45
	300	2.53	3.82	3.36	1.62	1.25	1.48	0.71	0.75	0.78
	400	3.62	5.20	4.30	2.09	1.57	1.86	1.25	1.06	1.05
	500	4.65	5.86	5.12	2.50	2.29	2.20	1.91	1.27	1.23
$S_{mr}(\Delta w_1 + \Delta w_2)$ [%]	200	97	68	86	99	100	100	100	100	100
	300	77	14	75	85	98	37	100	100	100
	400	14	9	18	63	87	20	65	78	96
	500	6	7	10	21	70	16	25	62	75
$\tan(\alpha)$ [$\times 10^3$]	200	2.3	5.5	4.4	2.3	1.5	2.0	1.2	1.8	0.6
	300	3.4	10.7	5.6	4.4	2.4	5.4	3.6	3.9	3.4
	400	5.2	8.3	9.3	6.5	4.8	6.0	6.3	6.1	5.0
	500	7.1	13.6	14.7	8.4	5.2	3.7	8.5	7.3	6.5

surfaces, while equivalent square root functions can describe Abbot-Firestone curves for bridges with open sections. Measured surface of Bridge #5 is an exception in box section bridges since the curves are more similar to those evaluated for open sections. The explanation of differences can be, that the measured zone belongs to an end support region without bending moment. On the other hand, minimum secant slope is larger for box section bridges.

The current paper uses a novel approach in the field of bridge engineering; the analogy of Abbott-Firestone curve, which is assessed for each measurement scenario to analyse the deformed shape near the structural bearing. It can be concluded that specific surface profile parameters such as normalized maximum out-of-flatness (using the norm of permitted total deformation limit in EN 1337–2), bearing area evaluated at $\Delta w_1 + \Delta w_2$, and the minimum secant slope are adequate and particularly useful for describing surface profiles for deformed steel plates in the vicinity of reaction forces since solely the magnitude of out-of-flatness is not inevitably sufficient for classifying surfaces in point of structural bearings. Furthermore, it can be concluded that cross-section type, and thickness of bottom flange and stiffeners have major influence on out-of-flatness in the vicinity of supports, while an unequivocal correlation between imperfections and erection period (i.e., development of manufacturing technology in the last decades) cannot be established based on actual measurements performed on steel and composite bridges constructed recently and in the 20th century in Central Europe bridges. Finally, it can be also concluded by analysing the three characteristic parameters of Abbott-Firestone curves that out-of-flatness is most critical in the case of internal supports of Bridge #2. Therefore, the superstructure of the aforementioned bridge is analysed

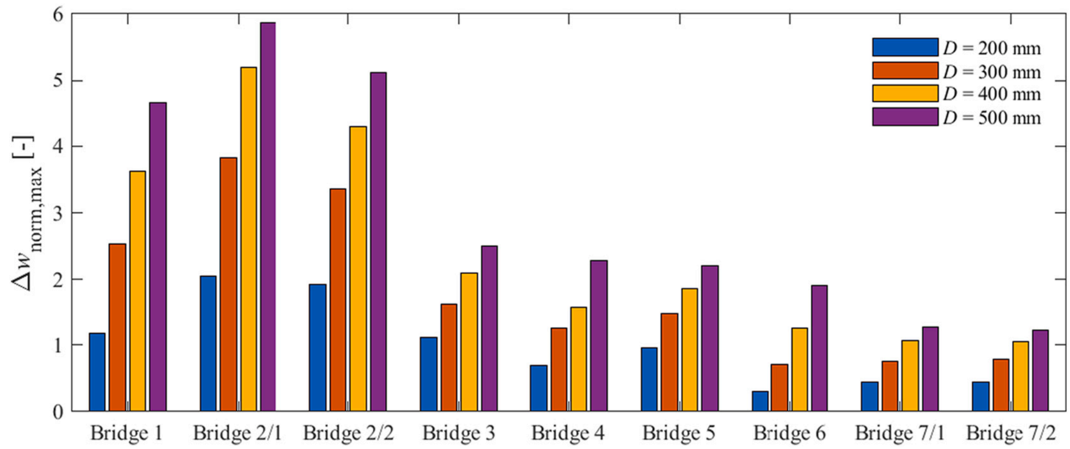

Fig. 10. Maximum normalized out-of-flatness [−] results for all the analysed bridges.

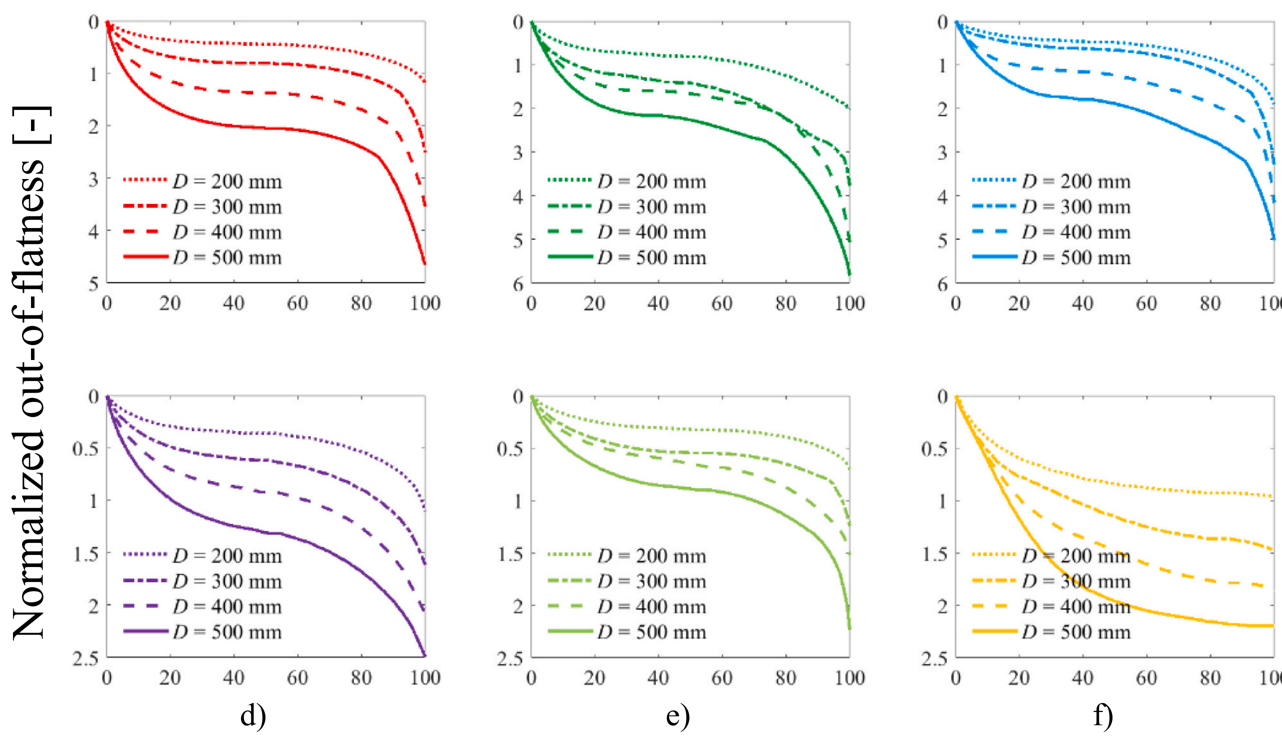

Fig. 11. Normalized Abbott-Firestone curves for bridges with box section: a) Bridge #1, b-c) Bridge #2, d) Bridge #3, e) Bridge #4 and f) Bridge #5.

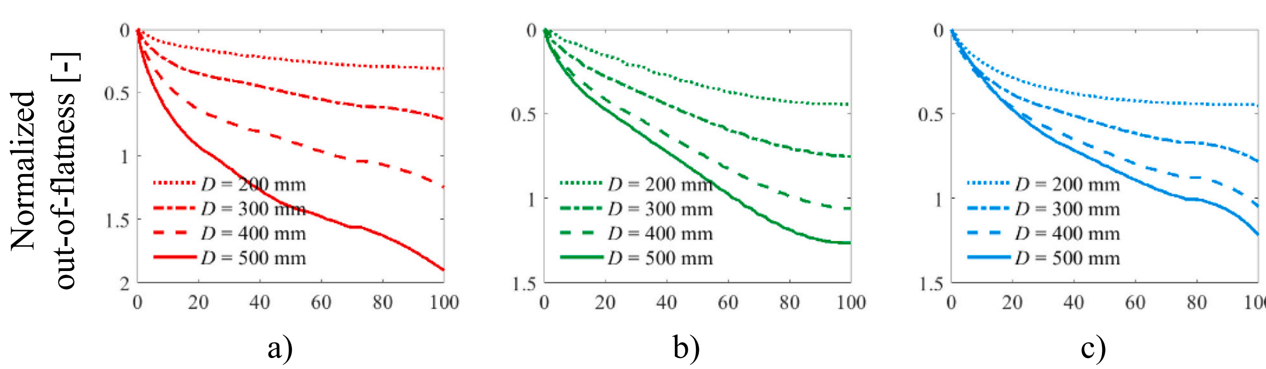

Fig. 12. Normalized Abbott-Firestone curves for bridges with open section: a) Bridge #6 and b-c) Bridge #7 (internal and end support).

in detail in the next section using welding simulation in order to understand the influence of different parameters on geometrical imperfections.

3. Numerical model development

Qualitative manufacturing simulation is carried out in addition to site measurements in order to analyse the influence of welding in the vicinity of structural bearings during the assembly and strengthening of a typical superstructure, while the effect of stiffness is evaluated as well using different bottom flange thicknesses. Additional manufacturing processes such as thermal cutting, cold-forming, etc. are ignored in the simulation since welding has the most significant effect on manufacturing-induced distortions. A comprehensive numerical model is developed in ANSYS, a general-purpose finite element software, in order to predict welding-induced temperature fields, residual stresses and distortions. Only typical welding variables are lumped heat inputs are used in welding simulations of a more than 30-year-old bridge segment since Welding Procedure Specifications (WPS) are not available. Thus, a qualitative comparison can be made with measurement results and geometrical imperfection shapes covered by EN 1090–2 standard. On the contrary, quantitative welding simulation can be performed (e.g., [33,34]) when details of welding technology are accessible.

Dimensions of the modelled subassembly is shown in Fig. 13. Modelled plate thickness is t_f = 16 mm (and 30 mm for a stiffer configuration) for the bottom flange and 30 mm for the diaphragm and bearing stiffeners above the support (i.e., structural bearing), while the longitudinal stiffener assumed to have a thickness of 8 mm and the web thickness is equal to 16 mm. Transverse bearing stiffeners, with plate thickness of 30 mm, are additionally modelled for optional strengthening and thus for demonstrating the variation of out-of-flatness imperfections in the case of retrofitting due to installing new structural bearing or increase of traffic load. Therefore, four configurations are simulated:

- Model #1: without additional transverse bearing stiffeners, t_f = 16 mm,
- Model #2: with additional transverse bearing stiffeners, t_f = 16 mm,
- Model #3: without additional transverse bearing stiffeners, t_f = 30 mm,
- Model #4: with additional transverse bearing stiffeners, t_f = 30 mm.

Three-dimensional transient uncoupled thermo-mechanical analysis is performed to simulate fusion welding processes. Linear solid elements are used in the simulation since smaller low-order elements perform better than larger high-order elements in nonlinear problems [35]. Eight-node solid elements, SOLID70 and SOLID185, are used in the finite element model. Solid elements with pure displacement formulation and full integration with B-bar method (also known as selective reduced integration method) are used in the vicinity of the welds in the mechanical analysis, while elements with enhanced strain formulation are applied in the remaining domains. A qualitative distortion analysis is carried out; therefore, plane of symmetry is defined at the diaphragm in order to model only the half of the subassembly and reduce computational time. Finite element mesh is shown in Fig. 14 for the entire subassembly for visualization purposes. A finer mesh is used in the vicinity of the welds both in the cross section and along the weld axis. Mesh sensitivity analysis is carried out, regarding maximum total distortions, in order to verify the applied mesh scheme. In general, two to eight finite elements are used through the thickness of plates. Cross-sectional element size is 1–2 mm in the vicinity of the welds, while average element size is ~15–20 mm far from weld beads. Average finite element size along weld axes is ~10–15 mm. Prism elements (degenerated shapes of 8-node elements in the software) are used between regions with finer and courser meshes in order to model continuity. The total

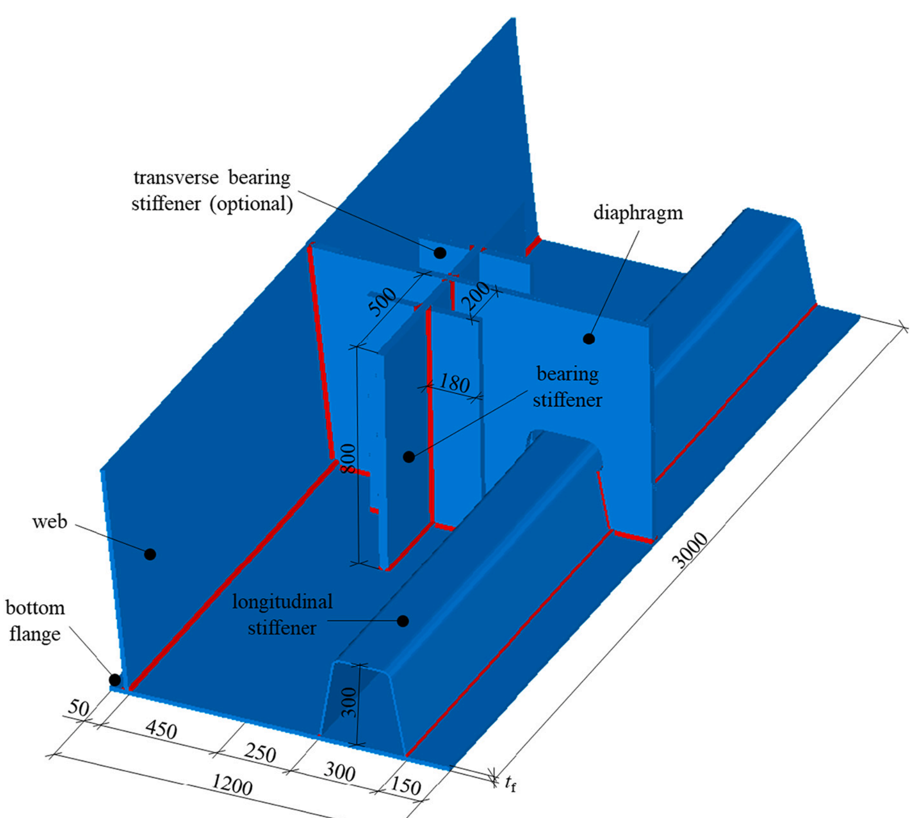

Fig. 13. Dimensions [mm] of the modelled subassembly.

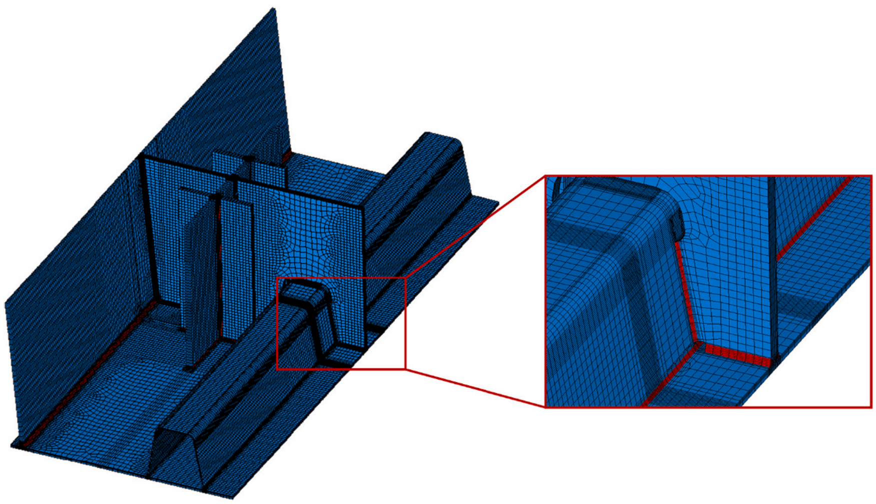

Fig. 14. Finite element mesh of the modelled subassembly.

number of nodes and elements for half of the subassembly are 179,244 and 149,230, respectively.

Temperature-dependent thermal and mechanical material properties (Fig. 15) are based on EN 1993-1-2 in the thermo-mechanical analysis. Material properties are defined below 1200 °C in the standard; however, temperature of the weld pool is much higher during welding. Therefore, material properties in general are set as constant values above the cut-off temperature. On the one hand, latent heat L = 270,000 J/kg due to melting and solidification is taken into account in enthalpy between solidus and liquidus temperatures, which are assumed to be 1440 °C and 1505 °C, respectively. On the other hand, increased equivalent thermal conductivity, according to [36], is applied in the simulations above the liquidus temperature in order to model convective heat transfer in the weld pool due to fluid flow. EN 1993-1-2 uses reduction factors for defining temperature-dependent Young's modulus, yield strength and stress-strain curves. The material model has a notable advantage as only yield strength (f_y = 355 MPa is assumed for structural steel grade S355) and Young's modulus (E = 210 GPa) are needed to be added at room temperature to describe the mechanical behaviour of the material. Required parameters are given in Annex A of EN 1993-1-2 to describe the stress-strain curves at elevated temperatures. A multilinear isotropic hardening model is used in the simulations with von Mises yield criterion and associative flow rule. Thermal strains are considered according to the Eurocode; however, reference temperature is 20 °C for base material and 1200 °C for melted material.

Filler material addition is modelled in the developed ANSYS code with the combination of 'birth and death' and 'quiet element' techniques in order to deal with melting, solidification, and activation of components during the assembly. The so-called 'birth and death' procedure is used in the thermal analysis for inactive components and weld passes, which means that the stiffness matrix (i.e., thermal conductivity) is multiplied by 10^{-6} by default for deactivated elements. In the mechanical analysis, the 'quiet element'technique is implemented since all elements are active from the beginning of the calculation. Young's modulus of 1000 MPa is used for not yet deposited or melted material, while linear thermal expansion coefficient is taken as zero to ensure thermal strain free bead elements before welding.

Boundary conditions are defined for both thermal and mechanical analyses. Initial temperature is 20 °C, while nodal temperatures of not yet deposited weld passes are prescribed in the first step of the calculation to avoid ill-conditioned matrices during heat flow calculations. Heat losses at the free surfaces are governed by radiation and convection. Film coefficient is assumed to be 25 W/(m^{2}K), emissivity is taken as a temperature-independent value with a magnitude of 0.8, while interpass temperature is 250 °C. Forced cooling is implemented in the last time step of the analysis to reach the ambient temperature. Welding heat sources induce heat generation which is defined as element body force load during the three-dimensional transient thermal analysis. The double ellipsoidal heat source model introduced by Goldak et al. [37] is implemented in the numerical framework, while an automated Frenet-Serret frame is used for modelling the movement of heat sources [38]. *Eqs.* 1 and 2 determine the power density distribution in the front and rear quadrants for a double ellipsoidal heat source model, respectively.

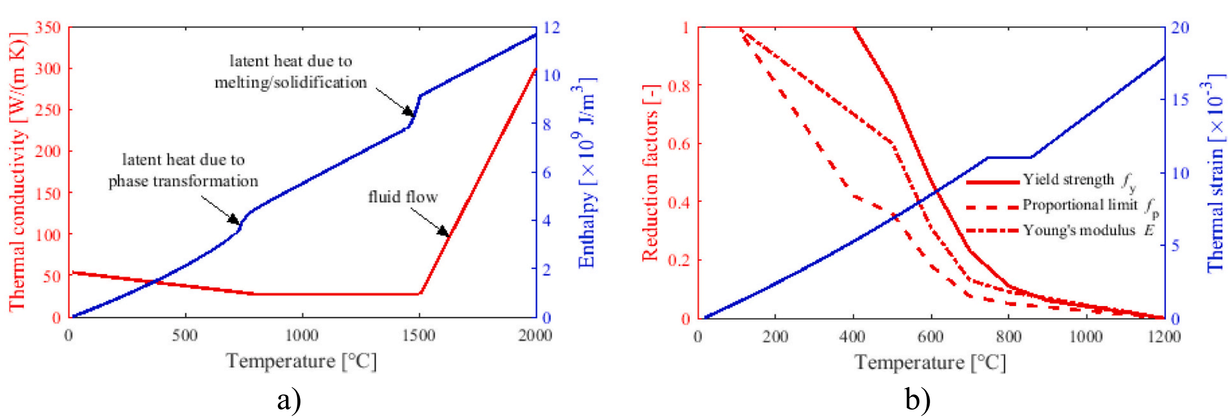

Fig. 15. a) Thermal and b) mechanical material properties for welding simulation.

$$q_{f}(x,y,z) = q_{max}\cdot e^{-3\frac{x^2}{c_f^2}-3\frac{y^2}{a^2}-3\frac{z^2}{b^2}} \quad (1)$$

$$q_{r}(x,y,z) = q_{max}\cdot e^{-3\frac{x^2}{c_r^2}-3\frac{y^2}{a^2}-3\frac{z^2}{b^2}} \quad (2)$$

where characteristic parameters c_f, c_r, b and a represent the physical dimensions of the heat source model in each direction as shown in Fig. 16. Temperature fields are applied as nodal loads in the mechanical analysis. On the one hand, weak springs ($k = 1$ N/mm) are added to all the plates in order to avoid rigid body motion during activation and deactivation of components, while additional mechanical boundary conditions are shown in Fig. 17. Since a qualitative distortion analysis is carried out, plane of symmetry is defined in both thermal (no heat flux) and mechanical analyses (displacement constraints) in order to model only the half of the subassembly and decrease total number of degrees of freedom (DOF); i.e., computational time is efficiently reduced without the loss of relevant information regarding the welding-induced distorted shape.

Sparse solver is used with implicit time integration scheme in nonlinear mechanical and transient thermal analyses with full Newton-Raphson method. Large deflection effects are included in the mechanical analysis. Background and additional details of the developed manufacturing framework can be found in [38].

Global welding sequence, which is identical with joint numbering, welding directions and main steps of the assembly are shown in Fig. 18. First, the longitudinal stiffener is welded to the bottom flange with single-bevel groove welds (Joint #1, simultaneous welding, web is inactive in Step #1). In Step #2, the joint of the web and bottom flange is welded with double-sided fillet weld (Joint #2, simultaneous welding). Then, the diaphragm is welded to the bottom flange and web plate in Step #3 using double-bevel groove welds (only one half is modelled due to symmetry). At first, the 1st weld passes of each joint are laid (Joints #3, #4 and #5, respectively) followed by the 2nd and 3rd weld passes. Finally, the joint between the longitudinal stiffener and diaphragm is welded assuming single-sided fillet welds with fillet size of 4 mm (Joint #6, simultaneous welding). Bearing stiffener above the support is simulated with double-bevel groove welds (Joints #7 and #8, respectively), while the transverse bearing stiffeners are modelled as retrofitting with single-bevel groove welds (Joints #9 and #10, respectively) due to accessibility of the joints. The modelled joints, schematic joint design and local welding sequence of multi-pass welds, net heat input q_{net}, travel speed v, welding process and corresponding characteristic heat source parameters (a, b, c_f and c_r) are summed up in Table 5. Metal active gas welding (MAG) and submerged arc welding (SAW) processes are considered in the simulations. Thermal efficiency η is set to 1.00 for submerged arc welding and it is 0.80 for metal active gas welding according to EN 1011–1 in the net heat input calculation ($q_{net} = \eta UI/v$). Lumped weld passes are considered in the finite element analysis in several joints as a simplification approach to reduce computational time;

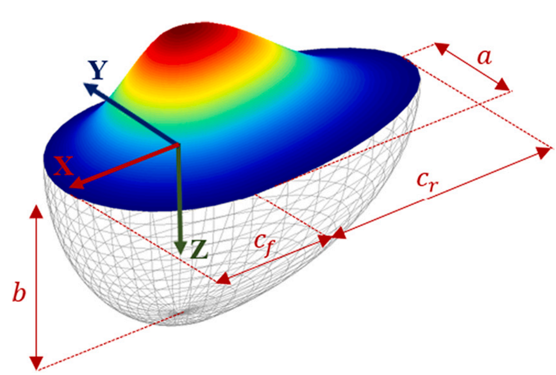

Fig. 16. Notations and power density distribution of the double ellipsoidal heat source model.

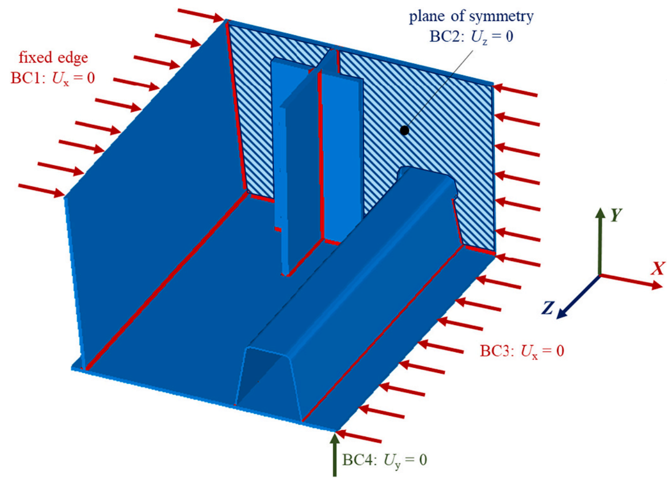

Fig. 17. Mechanical boundary conditions (red, green and blue arrows denote U_x, U_y and U_z constraints, respectively). (For interpretation of the references to colour in this figure legend, the reader is referred to the web version of this article.)

however, the essential phenomena resulting in residual distortions are taken into account in the qualitative modelling procedure.

4. Numerical results

The most essential results of the qualitative manufacturing simulation are presented hereafter in this section. Major results of the transient thermal analysis are temperature fields which are mapped to the finite element mesh and applied as nodal loads in the subsequent mechanical analysis. Transient temperature field and von Mises thermal stresses for a relevant step (Step #3) during the assembly are shown in Fig. 19 at the same time step when the 3rd weld passes of the double-bevel groove weld are welded in Joint #5 between the diaphragm ($t_1 = 30$ mm) and the web of the main girder ($t_2 = 16$ mm) using net heat input $q_{net} = 2.38$ kJ/mm, travel speed $v = 300$ mm/s and heat source parameters $a = 5$ mm, $b = 15$ mm, $c_f = 10$ mm and $c_r = 40$ mm. Specified minimum and maximum contour values are 20 °C and the liquidus temperature $T_{liq} = 1505$ °C for the temperature field in order to show the weld pool size (denoted with red colour), whilst 0 and yield strength $f_y = 355$ MPa are used for contour interval in the case of von Mises thermal stresses, which clearly demonstrates yielded regions (denoted with grey colour) in the heat-affected zone.

A parametric analysis is carried out to analyse the influence of bottom flange thickness (t_f) and application of additional transverse bearing stiffeners in the case of retrofitting due to installing new structural bearing, increase of traffic load, corrosion, etc. Welding-induced residual stresses and total distortions are shown for the four simulated cases, with and without additional transverse bearing stiffeners using $t_f = 16$ mm and 30 mm, in *Figs. 20 and 21*. First of all, largest distortions and major high stress zones are observable for Model #2 which is reasonable since the smaller flange thickness is analysed and further bearing stiffeners are welded causing extra imperfections and residual stresses in the weldment. These figures unambiguously show welding of transverse bearing stiffeners may notably affect both stress state and deformed shape of the bottom flange. On the one hand, cross-sectional area of stiffened region increases, which is favourable for the superstructure. However, it is an unfavourable case regarding the structural bearing since the permitted total deformation limit given by EN 1337–2 may not be fulfilled resulting in higher wear and highly nonuniform stress distribution in the sliding elements which can reduce remaining service life.

Maximum simulated geometrical distortions of the bottom flange, mainly due to welding-induced angular distortions, are 3.6 mm, 4.2 mm,

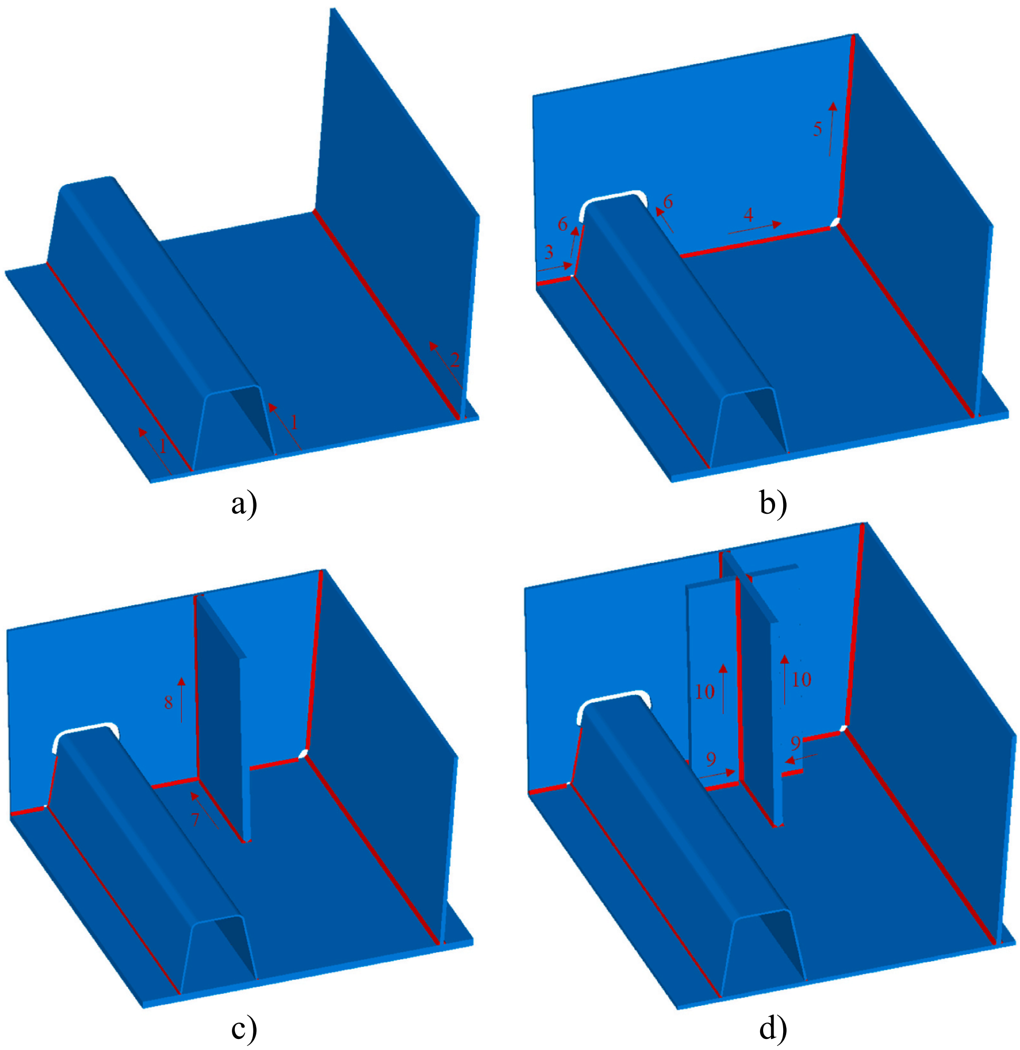

Fig. 18. Main steps of the assembly: a) Step #1 and #2, b-d) Steps #3–5.

1.9 mm, and 2.0 mm, respectively for Models #1–4. It is concluded that the effect of bottom flange thickness is significant. Maximum imperfections are halved by using a flange with $t_f = 30$ mm instead of $t_f = 16$ mm, while the difference between magnitudes for Models #1 and #2 without and with transverse stiffeners is 0.6 mm, which is comparable with permitted total deformation limit. However, the variance of imperfections is only 0.1 mm for Models #3 and 4 demonstrating the advantage of using thick flanges in the vicinity of supports even in the case of bridges with box sections instead of designing thin longitudinally stiffened plates where there is a need for installing mortar repeatedly or using new machined parts after strengthening operations on site. The most important simulated results are summarized in Table 6 similarly to measurement results including simulated maximum out-of-flatness ($\Delta w_{max,FEM}$), and maximum out-of-flatness-to-flange thickness ratio ($\Delta w_{max,FEM}/t_f$). The significance of bottom flange thickness is unambiguous. Model #2, with additional transverse stiffeners and bottom flange thickness $t_f = 16$ mm, corresponds to the submodel of an internal support of Bridge #2, where measured maximum out-of-flatness magnitudes are 4.8 mm and 5.2 mm, while simulated distortion is 4.2 mm. It has to be noted that only a qualitative analysis is performed since Welding Procedure Specifications are not available for the 30-year-old bridge. Parameters such as welding variables, welding sequence and fixtures during welding are only practical assumptions; however, a good agreement is achieved between measurement results and simulated imperfections. On the other hand, effect of reaction force is not considered in the numerical model which also increases out-of-flatness. Based on the authors' experience, magnitude of local deformations due to reaction force is ~0.1–0.5 mm for typical bridge superstructures.

Imperfection magnitudes are compared with the permitted total deformation limits ($\Delta w_1 + \Delta w_2$ according to *Eq. 1*) given by the standard, which are 0.53 mm, 0.61 mm, 0.66 mm and 0.70 mm for the assumed contact surfaces with diameters of $D = 200$ mm, 300 mm, 400 mm, and 500 mm, respectively. Results are evaluated in MATLAB; the approach of translational and rotational transformation, used for measurement results before, is applied for the simulated data set to find the three interfacing points representing each contact surface and determine out-of-flatness imperfections. The most important results for normalized out-of-flatness imperfections based on the numerical parametric analysis, in accordance with the methodology presented for measurement results, are summarized in Table 7 for the four analysed models, while normalized Abbott-Firestone curves are shown in Fig. 22. Maximum normalized out-of-flatness ($\Delta w_{norm,max,FEM}$) results, bearing areas ($S_{mr,FEM}$) evaluated at the permitted total deformation limit ($\Delta w_1 + \Delta w_2$), and minimum secant slopes ($\tan(\alpha_{FEM})$) are tabulated based on finite element modelling ('FEM'). It can be concluded that maximum normalized distortions, bearing areas and minimum secant slopes have an incoherent nature since the increase of evaluation diameter does not show an unequivocal tendency. However, nearly the total bearing area can be taken into consideration in service conditions for the models (Models #3 and #4) with flange thickness of 30 mm. Nevertheless,

Table 5
Welding parameters in finite element analysis (*t_2 = 30 mm in Models #3 and #4).

Joint #	Weld type	Joint design	t_1/t_2 ([mm/mm])	Weld pass #	Welding process	q_{net} [kJ/mm]	v [mm/min]	Heat source parameters [mm]			
								a	b	c_f	c_r
1	Single-bevel groove weld	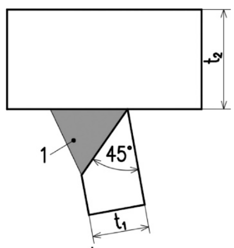	8/16*	1	SAW	2.475	400	6	12	10	40
2	Double-sided fillet weld	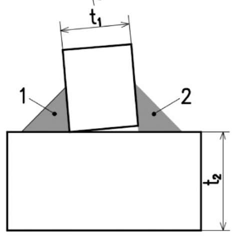	16/16*	1 & 2	SAW	3.15	400	9	9	10	40
3 4 5 7 8	Double-bevel groove weld	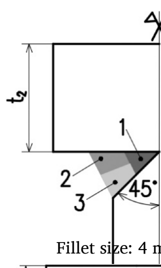	30/16* 30/16* 30/16* 30/16* 30/30	 1 2 3	MAG	 2.11 2.38 2.38	 300 300 300	 5 5 5	 10 15 15	 10 10 10	 40 40 40
6	Single-sided fillet weld	Fillet size: 4 mm	8/30	1	MAG	1.795	300	4	4	10	40
9 10	Single-bevel groove weld (optional strengthening)	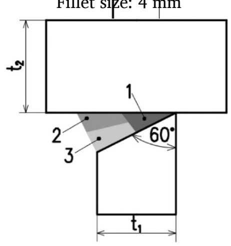	30/16* 30/30	1 2 3	MAG	2.53 3.80 3.80	300 200 200	6 6 6	18 18 18	10 10 10	40 40 40

welding of additional stiffeners substantially deteriorates the performance of the contact surface in Models #1 and #2, where flange thickness is 16 mm with a relatively low stiffness. On the one hand, bearing areas decrease for all the diameters comparing to Model #1 with a maximum reduction of 67%. On the other hand, using a larger structural bearing may not mean directly that it will have a better performance for service loads. The structural layout of the superstructure could have an out-of-flatness shape dramatically reducing bearing area due to welding of additional stiffeners. For instance, bearing area decreases from 69% to 28% when the assumed diameter of the contact area changes from 300 mm to 400 mm for Model #2.

The effect of welding additional transverse bearing stiffeners is evaluated in detail by deriving the difference of vertical distortions (Fig. 23), calculated without and with transverse bearing stiffeners, in order to highlight the effect of cumulative residual distortions during strengthening of the superstructure. Even mortar was installed, or a machined plate was used during the installation of the former structural bearing, the contact surface can be highly deformed after welding of additional parts, which highlights that wear resistance and service life of spherical structural bearings can be deteriorated by resulting in nonuniform stress distribution in the sliding elements.

Simulated out-of-flatness surfaces due to welding of transverse bearing stiffeners are presented in Fig. 24 for $t_f = 16$ mm and $t_f = 30$ mm assuming $D = 400$ mm. Magnitudes for these two cases are 0.85 mm and 0.60 mm. In accordance with evaluation of measurement results, corresponding normalized Abbott-Firestone curves (Fig. 25) are determined in order to classify the extent of defects for the simulated cases. Normalized magnitudes vary between 0.49÷1.14, and 0.32÷0.76, for t_f = 16 mm and t_f = 30 mm, respectively. Corresponding results are summarized in Table 8. Abbott-Firestone curve shapes do not change due to changing flange thickness, while maximum normalized out-of-flatness imperfection values are decreased effectively by ~30–35% for all the evaluated diameters. It can be concluded that, if only the effect of transverse stiffener is considered, maximum normalized distortions, and minimum secant slopes unambiguously increase when using larger contact areas. However, these results do not take the influence of reaction forces into account and assume that the initial distortions are managed to zero out before welding additional stiffeners. Main outcome

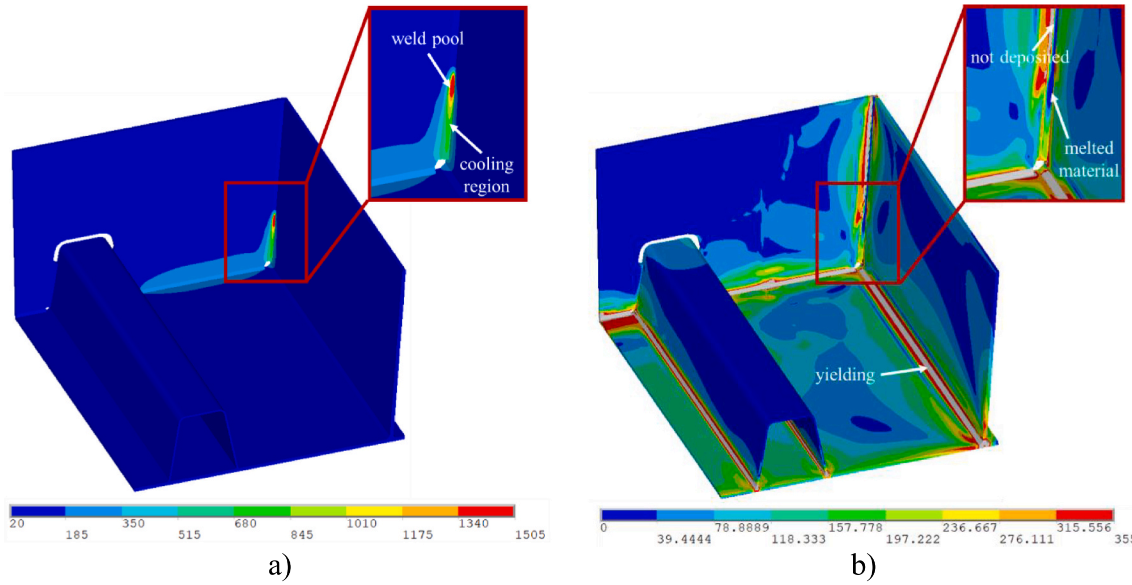

Fig. 19. a) Transient temperature field [°C] and b) von Mises thermal stresses [MPa] during the assembly (Step #3).

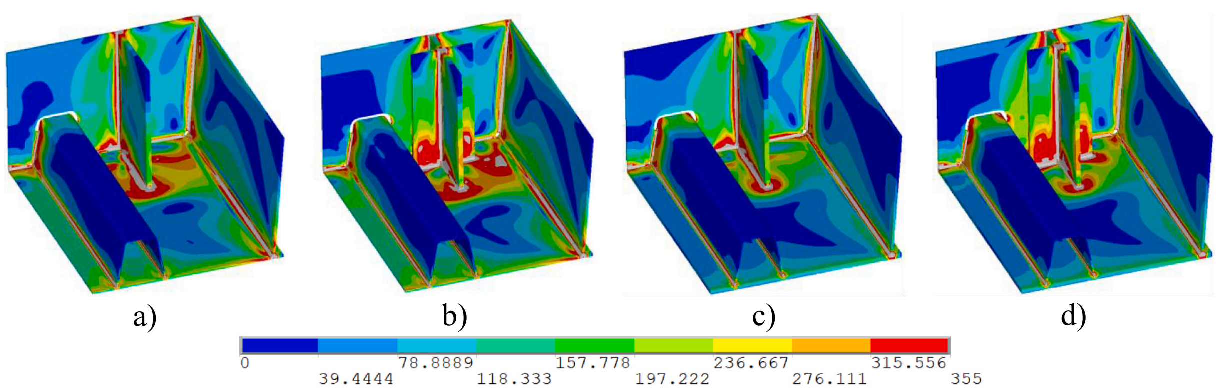

Fig. 20. Von Mises residual stresses [MPa] for a-d) Models #1–4.

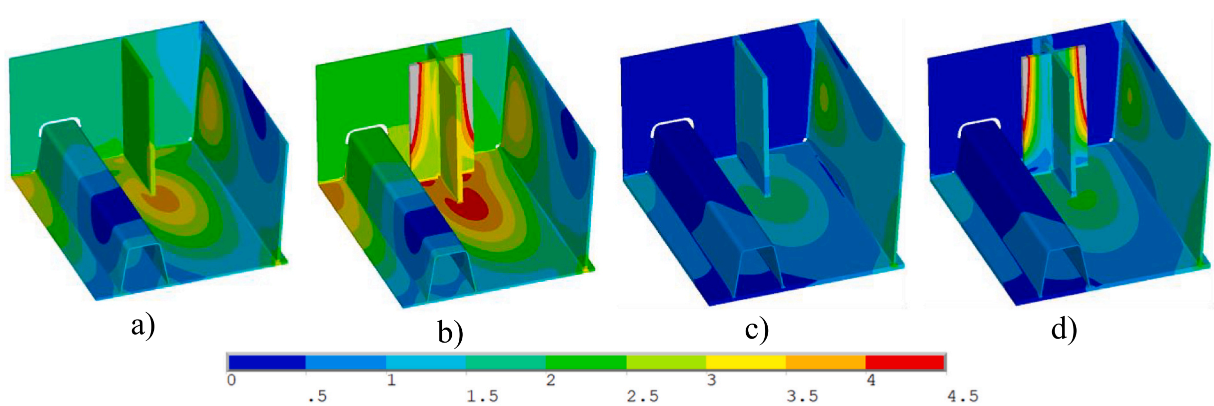

Fig. 21. Total distortions [mm] for a-d) Models #1–4.

of the obtained results is the need for installing mortar repeatedly or using new machined parts after such operations on site. It means, if additional bearing stiffeners are welded to a bridge structure after the bearing has been installed, out-of-flatness defects should be corrected again to eliminate failure or premature wear of the bearing system.

However, the extent of distortions can vary substantially and depends on welding technology and the layout of the superstructure. It is shown that thickness of bottom flange has substantial influence on out-of-flatness surface profile and ensuring permitted total deformation limit recommended by EN 1337–2. In addition, development of manufacturing technology using virtual simulations can have a beneficial effect on distortions.

Table 6
Out-of-flatness data of the numerical parametric analysis.

Data	Model #1	Model #2	Model #3	Model #4
t_f [mm]	16	16	30	30
additional stiffener	no	yes	no	yes
$\Delta w_{max,FEM}$ [mm]	3.6	4.2	1.9	2.0
$\Delta w_{max,FEM}/t_f$ [−]	0.225	0.263	0.063	0.067

Table 7
Normalized out-of-flatness results of contact surfaces based on simulations – distortions due to welding of the entire assembly.

Data	D [mm]	Model #1	Model #2	Model #3	Model #4
$\Delta w_{norm,max,FEM}$ [−]	200	1.30	1.27	0.40	0.77
	300	0.96	1.12	0.76	0.90
	400	1.04	1.36	0.54	1.00
	500	1.20	1.28	0.64	1.07
$S_{mr,FEM}(\Delta w_1 + \Delta w_2)$ [%]	200	50	40	100	100
	300	100	69	100	100
	400	95	28	100	100
	500	80	42	100	98
$\tan(\alpha_{FEM})$ [$\times 10^3$]	200	5.7	3.1	1.2	2.2
	300	8.0	3.3	1.6	3.5
	400	7.1	3.0	1.6	4.9
	500	6.8	4.0	1.7	5.6

5. Conclusions

Wear resistance and service life of spherical structural bearings can be increased by ensuring quasi uniform stress distribution in the sliding elements. Otherwise, both stress state and deformed shape of the bottom flange are unfavourably affected. Therefore, the present paper deals with out-of-flatness imperfections of bottom flanges in bridge superstructures due to manufacturing using measurements and welding simulations. The presented results are relevant for both constructional and design engineers. Out-of-flatness results are evaluated in accordance with the permitted total deformation limit in EN 1337–2 in the vicinity of the spherical structural bearing supports in order to clarify and highlight the importance of installing mortar or using machined plates with permitted out-of-flatness. A comprehensive numerical model is developed, and qualitative manufacturing simulation is carried out in ANSYS, a general-purpose finite element software in addition to site measurements to analyse the influence of welding in the vicinity of structural bearings during the assembly and strengthening of typical superstructures. The main findings of the paper are the following:

- The analogy of Abbott-Firestone curve, in accordance with normalization of out-of-flatness results based on permitted total deformation limit of EN 1337–2, is assessed for each measurement scenario to describe the deformed shape of the contact area. It is a novel application of an established approach in the field of bridge engineering for evaluating such a problem.
- Specific surface roughness parameters such as material ratio (bearing area) at a specified out-of-flatness and minimum secant slope are particularly useful in evaluating the extent of defects in the contact area. The magnitude of out-of-flatness is not inevitably sufficient for classifying contact surfaces.
- A qualitative comparison is made showing that the magnitudes and shapes of simulated and measured distortions are in good agreement.

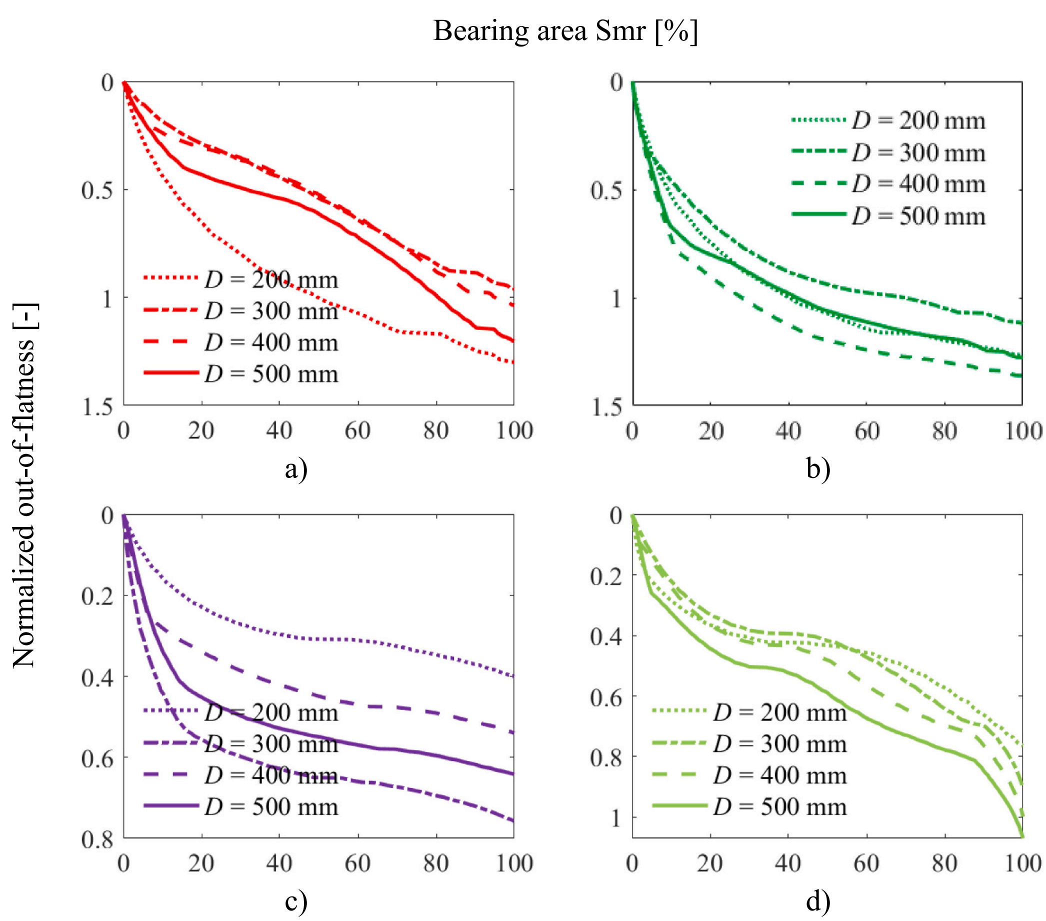

Fig. 22. Normalized Abbott-Firestone curves for a-d) Models #1–4.

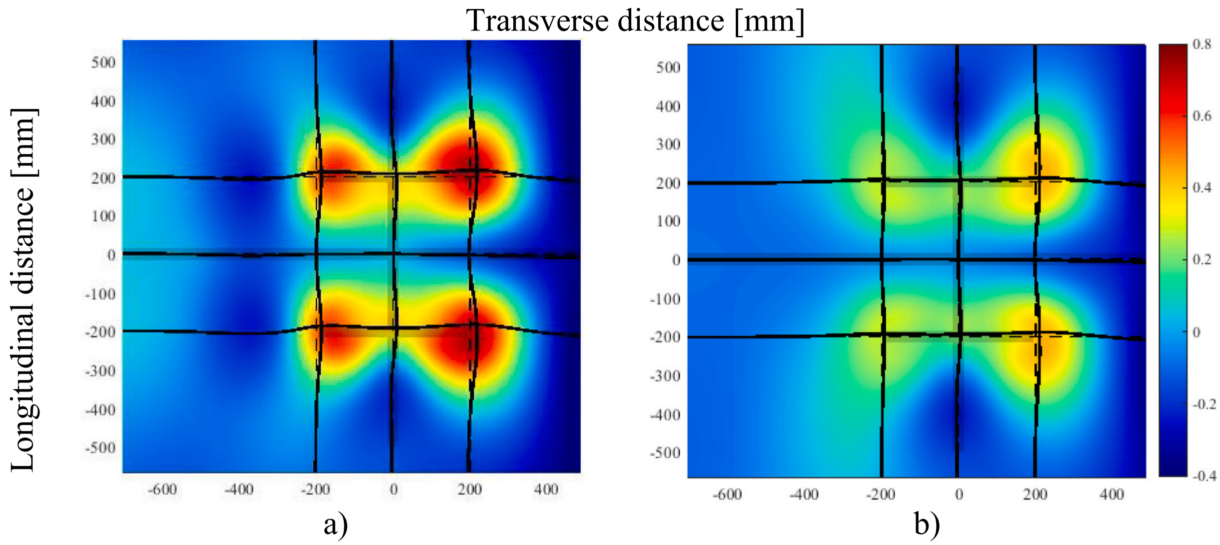

Fig. 23. Difference of vertical displacement fields [mm] in the vicinity of the support for a) $t_f = 16$ mm (Model #2-#1) and b) $t_f = 30$ mm (Model #4-#3).

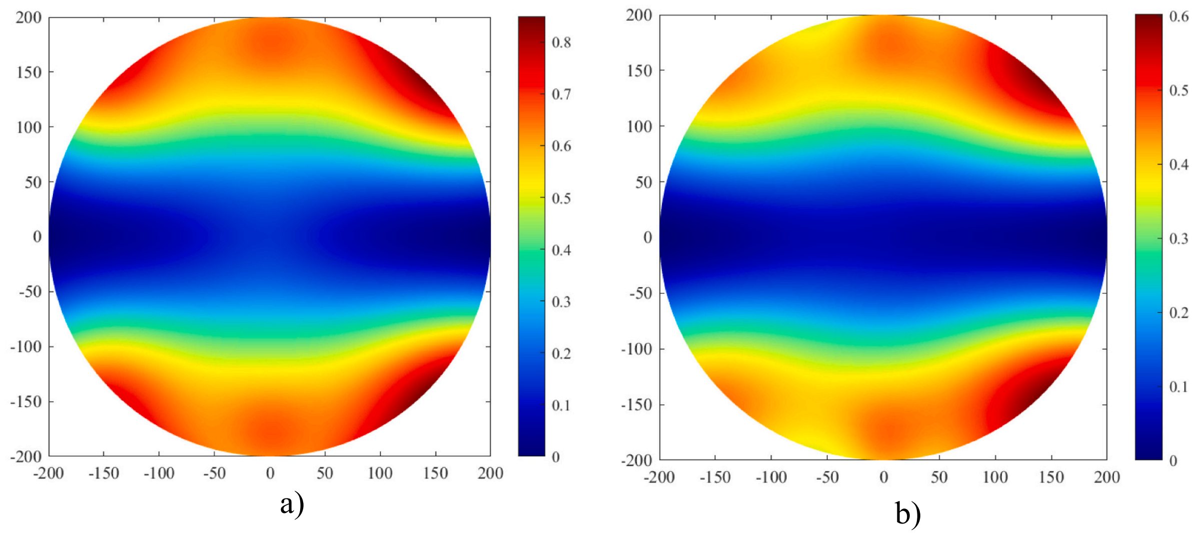

Fig. 24. Out-of-flatness imperfections [mm] due to additional stiffeners based on simulations for a) $t_f = 16$ mm and b) $t_f = 30$ mm, D = 400 mm, and $\Delta w_1 + \Delta w_2 = 0.66$ mm.

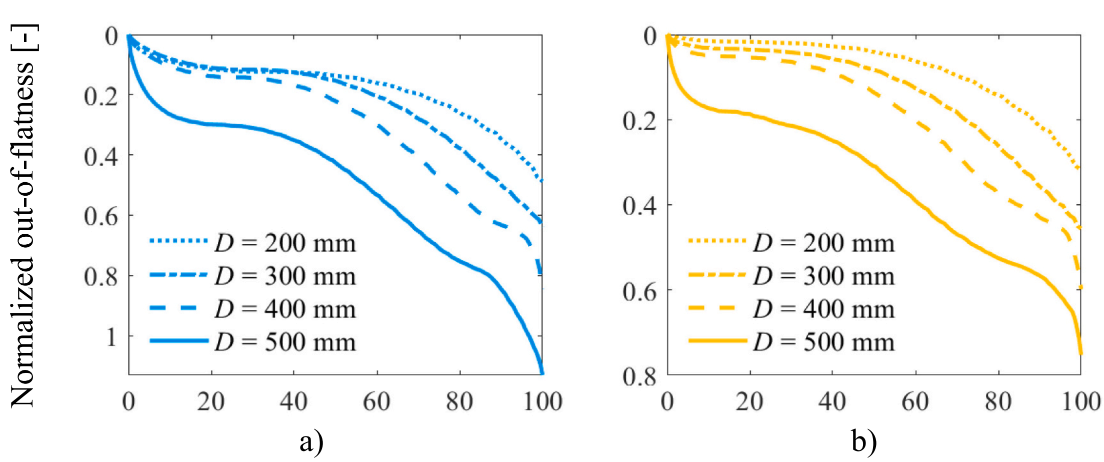

Fig. 25. Normalized Abbott-Firestone curves due to additional stiffeners based on simulations for a) $t_f = 16$ mm and b) $t_f = 30$ mm.

Table 8
Normalized out-of-flatness results of contact surfaces based on simulations – distortions due to welding of additional stiffeners.

Data	D [mm]	Model #2-#1	Model #4-#3
$\Delta w_{\mathrm{norm,max,FEM}}$ [−]	200	0.49	0.32
	300	0.64	0.46
	400	0.85	0.60
	500	1.14	0.76
$S_{\mathrm{mr,FEM}}(\Delta w_1 + \Delta w_2)$ [%]	200	100	100
	300	100	100
	400	100	100
	500	97	100
$\tan(\alpha_{\mathrm{FEM}})$ [$\times 10^3$]	200	1.0	0.5
	300	1.8	1.1
	400	2.8	1.7
	500	4.0	3.2

- Manufacturing simulation can be a powerful tool for improving welding technology or evaluating imperfections near the supports using virtual specimens instead of performing laborious and costly site measurements.
- It is demonstrated that using additional transverse bearing stiffeners for strengthening the superstructure results in larger distortions and smaller bearing areas. Even the magnitude of out-of-flatness due to welding only transverse bearing stiffeners can exceed the permitted limit resulting in nonuniform stress distribution in the sliding elements affecting wear resistance and service life of spherical structural bearings.
- Larger structural bearings may not mean directly that a better performance will be ensured for service loads. The structural layout of the superstructure could have an out-of-flatness shape dramatically reducing bearing area e.g., due to welding of additional stiffeners.

The future aim of the authors is to investigate the effect of imperfect bottom flanges on the behaviour and resistance of typical superstructures and structural bearings. The predicted imperfections can be used in virtual specimens to perform life-cycle assessment and evaluate damages by modelling the interaction of superstructure, structural bearing, and substructure. In addition, numerical modelling-based life-cycle assessment of the structural bearings could facilitate performing maintenance plans for bridges of particular importance.

CRediT authorship contribution statement

D. Kollár: Conceptualization, Methodology, Software, Data curation, Writing – original draft, Visualization. **B. Kövesdi:** Conceptualization, Methodology, Supervision, Writing – review & editing. **I. Völgyi:** Conceptualization, Methodology, Supervision, Writing – review & editing. **I. Biró:** Investigation, Resources, Conceptualization, Writing – original draft.

Declaration of Competing Interest

Authors declare that they have no conflict of interest.

Acknowledgement

The presented research program has been financially supported by the Grant MTA-BME Lendület LP2021-06/2021 "Theory of new generation steel bridges" program of the Hungarian Academy of Sciences,and the European Commission through the H2020 project EPIC under grant No. 739592. The research reported in this paper and carried out at the Budapest University of Technology and Economics has been supported by the National Research Development and Innovation Fund (TKP2020 Institution Excellence Subprogram, Grant No. BME-IE-WAT) based on the charter of bolster issued by the National Research Development and Innovation Office under the auspices of the Ministry for Innovation and Technology. Financial supports are gratefully acknowledged.

References

[1] EN 1337-1:2000, Structural Bearings – Part 1: General Design Rules, European Committee for Standardization, Brussels, Belgium, 2000.
[2] EN 1337-7:2004, Structural Bearings – Part 7: Spherical and Cylindrical PTFE Bearings, European Committee for Standardization, Brussels, Belgium, 2004.
[3] EN 1337-2:2004, Structural Bearings – Part 2: Sliding Elements, European Committee for Standardization, Brussels, Belgium, 2004.
[4] EN 1337-11:1997, Structural Bearings – Part 11: Transport, Storage and Installation, European Committee for Standardization, Brussels, Belgium, 1997.
[5] EN 1993-2:2006, Eurocode 3 - Design of Steel Structures - Part 2: Steel Bridges, European Committee for Standardization, Brussels, Belgium, 2006.
[6] R.J. Zhang, A.Q. Li, Finite element study of effect of parameters on stress distribution of steel shim in elastomeric bearings, Adv. Struct. Eng. 22 (2019) 2124–2135, https://doi.org/10.1177/1369433219834748.
[7] W. Wang, C. Li, K.L. Rens, C.L. Nogueira, Failure analysis of pot bearings in a curved viaduct, J. Perform. Constr. Facil. 34 (2020), https://doi.org/10.1061/(asce)cf.1943-5509.0001463.
[8] A.A. Adamov, A.A. Kamenskikh, Comparative analysis of the contact deformation of the spherical sliding layer of the bearing with and without taking into account the grooves with lubricant, IOP Conf. Ser. Mater. Sci. Eng. 581 (2019), https://doi.org/10.1088/1757-899X/581/1/012031.
[9] EN 1090-2:2018, Execution of steel structures and aluminium structures, in: Part 2: Technical requirements for steel structures, European Committee for Standardization, Brussels, Belgium, 2018.
[10] Vereinigung der Hersteller von Fahrbahn übergängen und Lagern für Bauwerke e. V. Information for construction sites, in: Insatllation of Bridge Bearings, 2010.
[11] S. Carmignato, E. Savio, Traceable volume measurements using coordinate measuring systems, CIRP Ann. - Manuf. Technol. 60 (2011) 519–522, https://doi.org/10.1016/j.cirp.2011.03.061.
[12] J.D. Carroll, P.E. Green, Linear transformations from a geometric viewpoint, in: J. D. Carroll, P.E. Green (Eds.), Math. Tools Appl. Multivar. Anal, Academic Press, San Diego, 1997, pp. 127–193.
[13] J. Santolaria, J.J. Aguilar, J.A. Yagüe, J. Pastor, Kinematic parameter estimation technique for calibration and repeatability improvement of articulated arm coordinate measuring machines, Precis. Eng. 32 (2008) 251–268, https://doi.org/10.1016/j.precisioneng.2007.09.002.
[14] B. Gapinski, M. Wieczorowski, L. Marciniak-Podsadna, B. Dybala, G. Ziolkowski, Comparison of different method of measurement geometry using CMM, optical scanner and computed tomography 3D, Procedia Eng. 69 (2014) 255–262, https://doi.org/10.1016/j.proeng.2014.02.230.
[15] A. Satyanarayana, M. Krishna, A. Chandrakanth, R. Pradyumna, Influence of LASER CMM process parameters on dimensional inspection of standard spheres, Mater. Today Proc. 5 (2018) 3965–3970, https://doi.org/10.1016/j.matpr.2017.11.654.
[16] A. Altinisik, E. Bolova, A comparison of off-line laser scanning measurement capability with coordinate measuring machines, Meas. J. Int. Meas. Confed. 168 (2021), 108228, https://doi.org/10.1016/j.measurement.2020.108228.
[17] G. Dai, S. Bütefisch, F. Pohlenz, H.U. Danzebrink, A high precision micro/nano CMM using piezoresistive tactile probes, Meas. Sci. Technol. 20 (2009), 084001, https://doi.org/10.1088/0957-0233/20/8/084001.
[18] D. Kollár, B. Kövesdi, L.G. Vigh, S. Horváth, Weld process model for simulating metal active gas welding, Int. J. Adv. Manuf. Technol. 102 (2019) 2063–2083, https://doi.org/10.1007/s00170-019-03302-3.
[19] A.R. Sousa, Metrological evaluation of a coordinate measuring machine with 5-axis measurement technology, Procedia CIRP. 75 (2018) 367–372, https://doi.org/10.1016/j.procir.2018.04.035.
[20] F. Zanini, L. Pagani, E. Savio, S. Carmignato, Characterisation of additively manufactured metal surfaces by means of X-ray computed tomography and generalised surface texture parameters, CIRP Ann. 68 (2019) 515–518, https://doi.org/10.1016/j.cirp.2019.04.074.
[21] D. Kim, Y. Kwak, H. Sohn, Accelerated cable-stayed bridge construction using terrestrial laser scanning, Autom. Constr. 117 (2020), 103269, https://doi.org/10.1016/j.autcon.2020.103269.
[22] R. Qin, A. Gruen, 3D change detection at street level using mobile laser scanning point clouds and terrestrial images, ISPRS J. Photogramm. Remote Sens. 90 (2014) 23–35, https://doi.org/10.1016/j.isprsjprs.2014.01.006.
[23] S. Piculin, P. Može, Experimental and numerical analysis of stiffened curved plates as bottom flanges of steel bridges, J. Constr. Steel Res. 164 (2020), 105822, https://doi.org/10.1016/j.jcsr.2019.105822.
[24] H. Pasternak, B. Launert, T. Kannengießer, M. Rhode, Advanced residual stress assessment of plate girders through welding simulation, Procedia Eng. 172 (2017) 23–30, https://doi.org/10.1016/j.proeng.2017.02.013.
[25] T. Krausche, B. Launert, H. Pasternak, A study on the prediction of welding effects in steel box girders, in: J. Jönsson (Ed.), Proc. Eurosteel, Ernst & Sohn Verlag, Berlin, 2017, pp. 4410–4416, https://doi.org/10.1002/cepa.500.
[26] E. Van Puymbroeck, G. Van Staen, N. Iqbal, H. De Backer, Residual weld stresses in stiffener-to-deck plate weld of an orthotropic steel deck, J. Constr. Steel Res. 159 (2019) 534–547, https://doi.org/10.1016/j.jcsr.2019.05.015.
[27] Q. Hua Zhang, Y. Ma, C. Cui, X. Yu Chai, S. Hui Han, Experimental investigation and numerical simulation on welding residual stress of innovative double-side welded rib-to-deck joints of orthotropic steel decks, J. Constr. Steel Res. 179 (2021), https://doi.org/10.1016/j.jcsr.2021.106544. Paper 106544.

[28] J. Wu, B. Qiang, X. Liao, L. Kang, C. Yao, Y. Li, Experimental investigation and numerical simulation of welding residual stress in orthotropic steel deck with diaphragm considering solid-state phase transformation, Eng. Struct. 250 (2022), 113415, https://doi.org/10.1016/j.engstruct.2021.113415.

[29] M. Hashemzadeh, Y. Garbatov, C. Guedes Soares, Hybrid-laser welding-induced distortions and residual stresses analysis of large-scale stiffener panel, Ocean Eng. 245 (2022), https://doi.org/10.1016/j.oceaneng.2021.110411. Paper 110411.

[30] EN ISO 10360-2:2009, Geometrical product specifications (GPS), in: Acceptance and Reverification Tests for Coordinate Measuring Machines (CMM) – Part 2: CMMs Used for Measuring Linear Dimensions, 2009.

[31] F.L. Bookstein, Principal warps: thin-plate splines and the decomposition of deformations, IEEE Trans. Pattern Anal. Mach. Intell. 11 (1989) 567–585, https://doi.org/10.1109/34.24792.

[32] E.J. Abbott, F.A. Firestone, Specifying surface quality: a method based on accurate measurement and comparison, Mech. Eng. 55 (1933) 569–572.

[33] C. Cui, Y. Bu, Y. Bao, Q. Zhang, Z. Ye, Strain energy-based fatigue life evaluation of deck-to-rib welded joints in OSD considering combined effects of stochastic traffic load and welded residual stress, J. Bridg. Eng. 23 (2018) 04017127, https://doi.org/10.1061/(asce)be.1943-5592.0001181.

[34] C. Cui, Q. Zhang, Y. Bao, S. Han, Y. Bu, Residual stress relaxation at innovative both-side welded rib-to-deck joints under cyclic loading, J. Constr. Steel Res. 156 (2019) 9–17, https://doi.org/10.1016/j.jcsr.2019.01.017.

[35] P. Michaleris, Minimization of Welding Distortion and Buckling, Woodhead Publishing Limited, Cambridge, 2011.

[36] J. Zhu, M. Khurshid, Z. Barsoum, Accuracy of computational welding mechanics methods for estimation of angular distortion and residual stresses, Weld. World. 63 (2019) 1391–1405, https://doi.org/10.1007/s40194-019-00746-9.

[37] J.A. Goldak, A. Chakravarti, M. Bibby, A new finite element model for welding heat sources, Metall. Trans. B 15 (1984) 299–305.

[38] D. Kollár, Welding Simulation in Advanced Manufacturing and Design of Steel Structures, Budapest University of Technology and Econimics, 2020.